

The Open University's repository of research publications  
and other research outputs

## Evolution of the Dust Size Distribution of Comet 67P/Churyumov–Gerasimenko from 2.2 au to Perihelion

### Journal Item

#### How to cite:

Fulle, M.; Marzari, F.; Della Corte, V.; Fornasier, S.; Sierks, H.; Rotundi, A.; Barbieri, C.; Lamy, P. L.; Rodrigo, R.; Koschny, D.; Rickman, H.; Keller, H. U.; López-Moreno, J. J.; Accolla, M.; Agarwal, J.; A'Hearn, M. F.; Altobelli, N.; Barucci, M. A.; Bertaux, J.-L.; Bertini, I.; Bodewits, D.; Bussoletti, E.; Colangeli, L.; Cosi, M.; Cremonese, G.; Crifo, J.-F.; Da Deppo, V.; Davidsson, B.; Debei, S.; De Cecco, M.; Esposito, F.; Ferrari, M.; Giovane, F.; Gustafson, B.; Green, S. F.; Groussin, O.; Grün, E.; Gutierrez, P.; Güttler, C.; Herranz, M. L.; Hviid, S. F.; Ip, W.; Ivanovski, S. L.; Jerónimo, J. M.; Jorda, L.; Knollenberg, J.; Kramm, R.; Kührt, E.; Küppers, M.; Lara, L.; Lazzarin, M.; Leese, M. R.; López-Jiménez, A. C.; Lucarelli, F.; Mazzotta Epifani, E.; McDonnell, J. A. M.; Mennella, V.; Molina, A.; Morales, R.; Moreno, F.; Mottola, S.; Naletto, G.; Oklay, N.; Ortiz, J. L.; Palomba, E.; Palumbo, P.; Perrin, J.-M.; Rietmeijer, F. J. M.; Rodríguez, J.; Sordini, R.; Thomas, N.; Tubiana, C.; Vincent, J.-B.; Weissman, P.; Wenzel, K.-P.; Zakharov, V. and Zarnecki, J. C. (2016). Evolution of the Dust Size Distribution of Comet 67P/Churyumov–Gerasimenko from 2.2 au to Perihelion. *The Astrophysical Journal*, 821(1), article no. 19.

For guidance on citations see [FAQs](#).

© 2016 The American Astronomical Society



<https://creativecommons.org/licenses/by-nc-nd/4.0/>

Version: Accepted Manuscript

Link(s) to article on publisher's website:

<http://dx.doi.org/doi:10.3847/0004-637X/821/1/19>

[oro.open.ac.uk](http://oro.open.ac.uk)

# Evolution of the dust size distribution of Comet 67P/Churyumov-Gerasimenko from 2.2 AU to perihelion

M. Fulle<sup>1</sup>

fulle@oats.inaf.it

F. Marzari<sup>2</sup>, V. Della Corte<sup>3</sup>, S. Fornasier<sup>4</sup>, H. Sierks<sup>5</sup>, A. Rotundi<sup>3,6</sup>, C. Barbieri<sup>7</sup>, P. L. Lamy<sup>8</sup>, R. Rodrigo<sup>9,10</sup>, D. Koschny<sup>11</sup>, H. Rickman<sup>12,13</sup>, H. U. Keller<sup>14</sup>, J. J. López-Moreno<sup>15</sup>, M. Accolla<sup>16</sup>, J. Agarwal<sup>5</sup>, M. F. A'Hearn<sup>17</sup>, N. Altobelli<sup>18</sup>, M. A. Barucci<sup>4</sup>, J.-L. Bertaux<sup>19</sup>, I. Bertini<sup>20</sup>, D. Bodewits<sup>17</sup>, E. Bussoletti<sup>6</sup>, L. Colangeli<sup>11</sup>, M. Cosi<sup>21</sup>, G. Cremonese<sup>22</sup>, J.-F. Crifo<sup>19</sup>, V. Da Deppo<sup>23</sup>, B. Davidsson<sup>12</sup>, S. Debei<sup>24</sup>, M. De Cecco<sup>25</sup>, F. Esposito<sup>26</sup>, M. Ferrari<sup>3</sup>, F. Giovane<sup>27</sup>, B. Gustafson<sup>28</sup>, S. F. Green<sup>29</sup>, O. Groussin<sup>8</sup>, E. Grün<sup>30</sup>, P. Gutierrez<sup>15</sup>, C. Güttler<sup>5</sup>, M. L. Herranz<sup>16</sup>, S. F. Hviid<sup>31</sup>, W. Ip<sup>32</sup>, S. L. Ivanovski<sup>3</sup>, J. M. Jerónimo<sup>15</sup>, L. Jorda<sup>8</sup>, J. Knollenberg<sup>31</sup>, R. Kramm<sup>5</sup>, E. Kührt<sup>31</sup>, M. Küppers<sup>18</sup>, L. Lara<sup>15</sup>, M. Lazzarin<sup>7</sup>, M. R. Leese<sup>29</sup>, A. C. López-Jiménez<sup>15</sup>, F. Lucarelli<sup>6</sup>, E. Mazzotta Epifani<sup>33</sup>, J. A. M. McDonnell<sup>29,34,35</sup>, V. Mennella<sup>26</sup>, A. Molina<sup>36</sup>, R. Morales<sup>15</sup>, F. Moreno<sup>15</sup>, S. Mottola<sup>31</sup>, G. Naletto<sup>20,24,37</sup>, N. Oklay<sup>5</sup>, J. L. Ortiz<sup>15</sup>, E. Palomba<sup>3</sup>, P. Palumbo<sup>6,3</sup>, J.-M. Perrin<sup>19,38</sup>, F. J. M. Rietmeijer<sup>39</sup>, J. Rodríguez<sup>15</sup>, R. Sordini<sup>3</sup>, N. Thomas<sup>40</sup>, C. Tubiana<sup>5</sup>, J.-B. Vincent<sup>5</sup>, P. Weissman<sup>41</sup>, K.-P. Wenzel<sup>11</sup>, V. Zakharov<sup>4</sup>, J. C. Zarnecki<sup>10,29</sup>

## ABSTRACT

The Rosetta probe, orbiting Jupiter-family comet 67P/Churyumov-Gerasimenko, is detecting individual dust particles of mass larger than  $10^{-10}$  kg by means of the GIADA dust collector and the OSIRIS WAC and NAC cameras since August, 2014, till September, 2016. Single dust particle detections allow us to estimate the anisotropic dust flux from 67P, infer the dust loss rate and size distribution at the sunlit nucleus surface, and look if 67P dust size distribution evolves in time. The Rosetta orbiter velocity, relative to 67P, is much lower than the dust velocity measured by GIADA, thus dust counts when GIADA is nadir-pointing will directly provide the dust flux. In OSIRIS observations, the dust flux is derived from the measurement of the dust space density close to the spacecraft. Under the assumption of radial expansion of the dust cloud, observations in the nadir direction provide the distance of the particles by measuring their trail length, with a parallax baseline determined by the motion of the spacecraft. The dust size distribution at sizes  $> 1$  mm observed by OSIRIS is consistent with a differential power index =  $-4$ , which was derived from models of the 67P trail. At sizes  $< 1$  mm, the size distribution observed by GIADA shows a strong time evolution, with a differential power index drifting from  $-2$  beyond 2 au, to  $-3.7$  at perihelion, in agreement with the evolution derived from coma and tail models based on ground-based data. The nucleus refractory-to-water mass ratio is close to six during the entire inbound orbit.

*Subject headings:* comets: general — comets: individual (67P/Churyumov-Gerasimenko) — space vehicles: instruments

---

<sup>1</sup>INAF – Osservatorio Astronomico, Via Tiepolo 11, I-34143 Trieste Italy

<sup>2</sup>Department of Physics, University of Padova, 35131, Padova, Italy

<sup>3</sup>INAF - Istituto di Astrofisica e Planetologia Spaziali, Via Fosso del Cavaliere, 100, 0133, Rome, Italy

<sup>4</sup>LESIA, Observatoire de Paris, PSL Research University, CNRS, Univ. Paris Diderot, Sorbonne Paris Cité, UPMC Univ. Paris 06, Sorbonne Universités, 5 Place J. Janssen, 92195 Meudon Principal Cedex, France

<sup>5</sup>Max-Planck-Institut für Sonnensystemforschung, Justus-von-Liebig-Weg, 3, 37077, Göttingen, Germany

<sup>6</sup>Università degli Studi di Napoli Parthenope, Dip. di Scienze e Tecnologie, CDN IC4, 80143, Naples, Italy

<sup>7</sup>Department of Physics and Astronomy, Padova University, Vicolo dell'Osservatorio 3, 35122, Padova, Italy

<sup>8</sup>Laboratoire d'Astrophysique de Marseilles, UMR 7326, CNRS & Aix Marseille Université, 13388 Marseilles Cedex 13, France

<sup>9</sup>Centro de Astrobiología (INTA-CSIC), 28691 Villanueva de la Canada, Madrid, Spain

<sup>10</sup>International Space Science Institute, Hallerstrasse 6, 3012, Bern, Switzerland

<sup>11</sup>ESA – ESTEC, Scientific Support Office, European Space Agency, Keplerlaan 1, 2201 AZ Noordwijk, The Netherlands

<sup>12</sup>Department of Physics and Astronomy, Uppsala University, Box 516, 75120, Uppsala, Sweden

<sup>13</sup>PAS Space Research Center, Bartycka 18A, PL-00716 Warszawa, Poland

<sup>14</sup>Institute for Geophysics and Extraterrestrial Physics, TU Braunschweig, 38106, Germany

<sup>15</sup>Instituto de Astrofísica de Andalucía (CSIC), Glorieta de la Astronomía s/n, 18008 Granada, Spain

<sup>16</sup>INAF – Osservatorio Astrofisico di Catania, Via Santa Sofia 78, 95123, Catania, Italy

<sup>17</sup>Department of Astronomy, University of Maryland, College Park, MD, 20742-2421, USA

<sup>18</sup>ESA-ESAC, Camino Bajo del Castillo, s/n., Urb. Villanueva del Castillo, 28692 Villanueva de la Canada, Madrid, Spagna

<sup>19</sup>LATMOS, CNRS/UVSQ/IPSL, 11 boulevard d'Alembert, 78280, Guyancourt, France

<sup>20</sup>University of Padova, CISAS, via Venezia 15, 35100 Padova, Italy

<sup>21</sup>Selex-ES, Via A. Einstein, 35, 50013 Campi Bisenzio FI, Italy

<sup>22</sup>INAF – Osservatorio Astronomico di Padova, Vicolo dell'Osservatorio 5, 35122, Padova, Italy

<sup>23</sup>CNR-IFN UOS Padova LUXOR, via Trasea 7, 35131 Padova, Italy

<sup>24</sup>Department of Mech. Engineering - University of Padova, via Venezia 1, 35131 Padova, Italy

<sup>25</sup>UNITN, Università di Trento, via Mesiano, 77, 38100 Trento, Italy

<sup>26</sup>INAF - Osservatorio Astronomico di Capodimonte,

## 1. Introduction

The size distribution of dust particles present on the nucleus or embedded in the first few meters below the surface is a fundamental parameter in various physical processes occurring on a comet. For instance, a different size distribution in the northern and southern comet hemi-nuclei, impacting the thermal properties and the porosity of the nucleus, may drive the outgassing time evolution. The dust size distribution can be measured by counting the pebbles on the surface (Mottola et al. 2015), or by measuring the dust flux in the coma using dust detectors, and using optical images of single particles (Rotundi et al. 2015). A comparison between these two size distributions, both defined at the nucleus surface, may allow us to infer information on the physical processes of competing dust release and dust fall-back onto the nucleus surface. In the case of 67P, these two size distributions maintain the same slope for particles

---

Salita Moiariello, 16, 80133, Naples, Italy

<sup>27</sup>Virginia Polytechnic Institute and State University, Blacksburg, VA 24061, USA

<sup>28</sup>University of Florida, Gainesville, Florida, 32611, USA

<sup>29</sup>Planetary and Space Sciences, Department of Physical Sciences, The Open University, Milton Keynes, MK7 6AA, UK

<sup>30</sup>Max-Planck-Institut fuer Kernphysik, Saupfercheckweg 1, 69117 Heidelberg, Germany

<sup>31</sup>Institute of Planetary Research, DLR, Rutherfordstrasse 2, 12489, Berlin, Germany

<sup>32</sup>Institute for Space Science, Nat. Central Univ., 300 Chung Da Rd., 32054, Chung-Li, Taiwan

<sup>33</sup>INAF - Osservatorio Astronomico di Roma, Via di Frascati, 33, Monte Porzio Catone, Rome, Italy

<sup>34</sup>The University of Kent, School of Physical Sciences, Canterbury, Kent, CT2 7NZ, UK

<sup>35</sup>UnispaceKent, Canterbury, Kent, CT2 8EF, UK

<sup>36</sup>Dep. de Física Aplicada, Universidad de Granada, Facultad de Ciencias, Avda. Severo Ochoa, s/n, 18071, Granada, Spain

<sup>37</sup>Dept. of Information Engineering – Padova University, via Gradenigo 6, 35131 Padova Italy

<sup>38</sup>Observatoire de Haute Provence OSU Pythas UMS 2244 CNRS-AMU, 04870 Saint Michel l'Observatoire, France

<sup>39</sup>Department of Earth and Planetary Sciences, MSC03 2040, 1–University of New Mexico, Albuquerque, NM 87131–0001, USA

<sup>40</sup>Physikalisches Institut, Sidlerstrasse 5, University of Bern, 3012, Bern, Switzerland

<sup>41</sup>Planetary Science Institute, 1700 East Fort Lowell, Suite 106, Tucson, AZ 85719, USA

ranging from 1 mm to a few meters: a differential power index =  $-3.8$  on smooth terrains at sizes above a few cm (Mottola et al. 2015) and a differential power index of  $-4$  for sizes below a few cm (Rotundi et al. 2015). The remarkable agreement between the slopes of the two distributions suggests that no significant selection processes affect either the dust release or the dust fall-back between sizes of 1 mm and a few meters. Dust release and fall-back, also defined as aeolian transfer of dust across the nucleus surface (Thomas et al. 2015), are time-dependent because they depend on the local gas loss rate from the nucleus surface. The local outgassing in turn depends on the local illumination of the nucleus surface, which depends on the nucleus topography, the heliocentric distance, and on the nucleus seasons due to the obliquity of the spin axis. This implies that also the surface dust size distribution extracted from data collected in the coma should strongly depend on time.

Inverse tail models (Fulle 2004) allow us to infer the time evolution of the dust size distribution from ground-based data. This model, applied to 2P/Encke (Epifani et al. 2001), has evidenced strong changes in the slope of the dust size distribution. In the time interval from 20 to 3 days before perihelion, the differential power index is constant at  $-3$ . Then, it jumps down to  $-4$ , and remains constant at  $-4$  up to 23 days after perihelion. Then, it jumps back to  $-3$ , and remains constant at  $-3$  during 3 months after perihelion. Comet 2P/Encke is one of the few Jupiter Family Comets with known equinox times, extracted by models of the nucleus non-gravitational forces. The equinoxes of comet 2P occur on 3 days before, and on 23 days after perihelion (Sekanina 1988). The dust size distribution of comet 2P is much steeper during the short summer at perihelion than during the longer aphelion winter, showing that the northern and southern hemi-nuclei of 2P/Encke are covered by dust of significantly different sizes. Models applied to ground-based observations indicate that comet 67P shows a similar behaviour, with the power index of the differential dust size distribution (at sizes  $< 1$  mm) changing from  $-3.0$  before, to  $-4.2$  after perihelion (Fulle et al. 2010). Comet 67P equinoxes occur at 1.7 au inbound, and at 2.6 au outbound. The ground-based data taken into account to extract

the time evolution of 67P size distribution (Fulle et al. 2010) stop at 2.6 au outbound. These facts indicate that a time evolution of 67P dust size distribution linked to the nucleus seasons (similar to what occurs for comet 2P/Encke) may be consistent with available ground-based data: 67P differential dust size distribution (at sizes  $< 1$  mm) may have a power index of  $-4.2$  during the short perihelion summer (from 1.7 au inbound to 2.6 au outbound), and a power index of  $-3.0$  during the long aphelion winter (from 2.6 au outbound to 1.7 au inbound).

The Rosetta mission, following 67P comet nucleus from August 2014 (3.6 au inbound) to September 2016 (3.6 au outbound), offers a unique opportunity to verify if 67P dust size distributions evolve in time, and if this evolution is due to 67P nucleus seasons. Detections of dust particles by the GIADA instrument (Colangeli et al. 2007), (Della Corte et al. 2014), and by the OSIRIS NAC camera (Keller et al. 2007) in 67P coma have already allowed us to measure the dust size distribution over 8 mass bins, from  $10^{-10}$  to  $10^{-2}$  kg when the comet was between 3.6 and 3.4 au inbound (Rotundi et al. 2015). The measurements have confirmed the predictions of tail models (Fulle et al. 2010): the dust size distribution shows a knee at about 1 mm (i.e. at about  $10^{-6}$  kg), with a differential power index of  $-4$  at sizes larger than 1 mm, and close to  $-2$  at smaller sizes. The bulk densities of the particles collected by GIADA, between  $10^3$  and  $3 \times 10^3$  kg m $^{-3}$ , suggest that most of the dust released from 67P consists of compact particles (Rotundi et al. 2015). Another smaller population of fluffy particles may account for about 15% of the coma brightness from  $10^{-11}$  to  $10^{-6}$  kg (Fulle et al. 2015), thus explaining the power index =  $-3$  obtained from ground-based observations (Fulle et al. 2010). GIADA data suggest a significant bulk density gap between the two populations: fluffy particles have densities even lower than 1 kg m $^{-3}$ , and have always been detected as short-lasting showers of single detections, resulting from the fragmentation of fragile parents at the interaction with the spacecraft electric field (Fulle et al. 2015).

In this paper, we extend the results obtained beyond 3.4 au inbound (Rotundi et al. 2015) analysing the measurements of GIADA and OSIRIS instruments from 2.2 au to perihelion, a

time period when 67P crossed the spring equinox. GIADA data have shown that in 67P the ejection of compact particles is strongly anisotropic: it is confined within the sunlit hemi-nucleus, thus maximised when the Sun–67P–Rosetta angle (phase angle  $\alpha$ ) is small (Della Corte et al. 2015). The Rosetta spacecraft has spent most of its time in terminator orbits ( $\alpha = 90$  deg), where the dust flux is much lower than at lower phase angles. In order to extract a significant dust loss rate, we consider here dust observations performed at phase angles  $\alpha < 90$  deg. The large nucleus–Rosetta distances maintained during most of 2015 implied very low dust fluxes at the spacecraft. Thus, good statistics of GIADA detections required integration periods at low phase angles at least a week long. We complement GIADA dust counts with detections of individual larger particles by OSIRIS cameras occurred during the same periods. All these conditions have been fulfilled during a few weeks in February (2.2 au inbound), in March 2015 (2.1 au inbound), and then at the end of August 2015 (perihelion, Tab. 1).

## 2. OSIRIS data

Photometry of individual dust particles detected by OSIRIS cameras provides their cross section (times the albedo times the phase function) if the particle distance can be determined by means of parallax. OSIRIS observations by means of the Narrow Angle Camera (NAC, pixel size = 3.8 arcsec) and Wide Angle Camera (WAC, pixel size = 20.5 arcsec) actually provide three independent parallax measurements, linked to three different baselines. The first baseline is the size of OSIRIS optics ( $\approx 0.1$  m): when a particle is closer than about 200 m in WAC images (about 1 km in NAC images), the particle appears out of focus, and the size of the out-of-focus spot provides the particle distance. The second baseline is the distance between the optical axes of WAC and NAC cameras ( $\approx 1$  m): when the same particle is detected at the same time by NAC and WAC, its distance is provided by its different position in NAC and WAC images with respect to field stars. These two first techniques sample a small coma volume around the spacecraft, too small to provide significant statistics at dust mass bins significantly larger than those sampled by GIADA. The third technique allows us to sample much

larger distances, but is based on the assumption that the dust motion is mostly radial from the nucleus, a condition that is usually satisfied in the sun-faced coma at small phase angles. If the dust motion is mostly radial from the nucleus, then observations performed in the nadir direction (usually with the nucleus itself in the image center) or in the anti-nadir direction minimize the apparent dust motion in the sky due to the dust velocity. In these conditions, most of the apparent dust motion is due to the spacecraft motion. The sky-projected spacecraft velocity  $v_{sc}$  (Tab. 1) provides the third parallax baseline, which is given by the OSIRIS exposure time times  $v_{sc}$ . Usually this baseline is much longer than those provided by the first two parallax techniques, and allows us to sample all the dust mass bins up to the largest ejected masses (Rotundi et al. 2015).

Nadir observations offer a further advantage. Since the nucleus is always present in the image, dust photometry can be measured in units of mean nucleus surface brightness. If we assume that the biggest dust particles and the nucleus surface have the same albedo times the phase function, then individual particle photometry, coupled to the distance determined by parallax, provides a direct estimate of the particle cross section. Observations of a large number of individual particles by means of this technique allow us to cancel out random deviations due to the non-radial dust motion from the nucleus surface, and due to different albedo between dust and nucleus. The small field of view of both NAC (2.2 deg) and WAC (11.6 deg) allows us to neglect effects due to the albedo phase function. We have identified the OSIRIS observation sequences named DUST–MON (MON means monitoring) as the best ones suited for this purpose. They consist of sets of pairs of images at the wavelength of 649 nm (NAC) and 613 nm (WAC): a long exposure (many seconds) where the particles are identified as long tracks, and a much shorter exposure wherein the dust particles appear as dots. The short exposure maximizes the S/N ratio of the particle over the diffuse coma background and allows us to best perform the dust photometry. A dust particle is identified in the difference image between long and short exposures if the corresponding track and dot lie on the same straight line, and if the ratio of the track length in the first exposure and the gap between the track

edge (long exposure) and the dot (short exposure) corresponds to the ratio between the track exposure time and the time interval between the two exposures. These two conditions ensure that we are observing the same dust particle in both exposures. Examples of difference images where single particle detections have been performed are shown in Figs. 1 and 2 (here the long track appears black and the dot – first exposure – appears white) and Fig. 3 (here the long track – first exposure – appears white and the dot appears black) for the observations listed in Tab. 1. This detection technique provides complete samples up to the faintest (i.e. smallest and closest) detected particles: the closer a particle, the longer and fainter its track on the long exposure image. NAC sequences can be used if  $R > 300$  km, otherwise most of the image is polluted by the nucleus and the brightest inner coma. WAC camera was not available after July, 2015.

The full list of single particle detections is shown in Tab. 2 (2.2 au inbound), Tab. 3 (2.1 au inbound), and Tab. 4 (perihelion). The particle brightness  $I$  is expressed in mean nucleus surface brightness units, and directly provides the radius  $r$  of the equivalent sphere scattering the observed brightness (the assumed geometric optical scattering is consistent with all the values  $r > 1$  mm):  $I b^2 = \pi r^2$ , where  $b$  is the pixel size at the particle distance. The size  $b$  is provided by the parallax equation  $a b \cos \beta = v_{sc}$ , where  $a$  is the measured particle apparent velocity in  $\text{px s}^{-1}$  units,  $v_{sc}$  is the spacecraft velocity projected on the sky, and  $\beta$  is the angle between the velocities  $v_{sc}$  and  $a$ . The angles  $\beta$  and  $\gamma$  (Tab. 2) allow us to estimate the dust radial velocity  $v$  by the equation  $v \tan \gamma = v_{sc} \sin \beta$ . The projection of the spacecraft velocity along the line of sight  $v_{scz}$  (Tab. 1) is always much smaller than the radial dust velocity, and has been neglected. The assumption that the dust velocity is mostly radial from the nucleus requires that the particles move outwards with respect to the nucleus in the OSIRIS images. This condition is verified for most particles at 2.1 and 2.2 au, but not in the perihelion images. This may be due to the higher phase angle  $\alpha$  (Tab. 1) at perihelion: close to terminator, the strong gradient of the gas density between nucleus day and night sides may introduce a significant tangential component in the dust velocity, directed towards the

nucleus night-side. In fact, most  $\beta$  values are positive (the Sun is in the upper direction of Figs. 1, 2 and 3). The dust velocities provided by OSIRIS observations are much more uncertain at perihelion than at 2.1 and 2.2 au. Most  $\beta$  values at all heliocentric distances are below 20 deg, showing that the assumption that most of the dust apparent motion is due to the sky-projected spacecraft motion is always satisfied.

In order to extract the 67P dust mass distribution, we have grouped the particle counts according to their mass. The results are shown in Tabs. 5, 6, 7 and 8. The number of counts per OSIRIS image pair and mass bin divided by the coma volume sampled by OSIRIS cameras provides the dust coma space density  $\rho$ . It depends on the largest distance  $D$  from the spacecraft at which a particle in each mass bin has been detected. This distance  $D$  is always much smaller than the spacecraft distance from the nucleus  $R$  (Tab. 1), so that the dust coma density between  $R - D$  and  $R$  can be assumed as a constant quantity. In this case, when we approximate the dust ejection from 67P nucleus as a sun-faced hemisphere, the dust number loss rate from the nucleus surface integrated in each mass bin is  $Q_n = 2\pi R^2 v \rho$ , where  $v$  is the mean dust velocity in each mass bin, and the dust mass loss rate (and mass distribution at the nucleus surface) is  $Q_m = m Q_n$ , where  $m$  is the mean dust mass in each mass bin. The 67P dust mass distribution is shown in Figs. 4, 5 and 6, for two values of the dust bulk density of  $10^3 \text{ kg m}^{-3}$  and  $3 \times 10^3 \text{ kg m}^{-3}$ , following the 67P dust bulk density estimates provided by the GIADA measurements (Rotundi et al. 2015). In each mass bin, we also compute the mean dust cross section  $\sigma$ , which allows us to compute the quantity  $Af\rho = 2A_p Q_n \sigma v^{-1}$ , where  $A_p = 0.065$  is the geometric nucleus albedo at 649 nm (Fornasier et al. 2015), which provides the coma brightness contribution of each mass bin. The integral of  $Af\rho$  over all the mass bins can be compared to the same quantity provided by ground-based observations, to check if the mass bins sampled by OSIRIS and GIADA instruments provide a dominant or negligible coma brightness contribution, or if the 67P size distribution changes from nucleus distances  $R$  to the outer coma observed from ground.

### 3. GIADA data

GIADA characterises individual dust particles by means of two independent sensors. At the instrument entrance the particle crosses a laser curtain, and is detected by photoelectric sensors (GDS, Grain Detection System) registering a signal (proportional to the particle cross-section times the albedo) and the laser curtain crossing time. Then the particle hits the Impact Sensor (IS, with the same GDS cross section,  $A = 10^{-2} \text{ m}^2$ ), which registers individual particle impact momentum and its travel time from GDS to IS. The combination of GDS and IS measurements (GDS+IS particles) provides the particle mass and velocity, and constrains the particle bulk density by means of calibration curves (Della Corte et al. 2016) derived on ground using cometary analogues (Ferrari et al. 2014). If the particle is too small to be detected by the GDS system, it may be detected by the IS sensor only (IS particles): in this case the particle momentum is converted to the mass assuming the mean value of the velocities of the GDS+IS particles in the same momentum bin, or assuming the velocities predicted by tail models (Fulle et al. 2010) if  $N_{gds+is} = 0$  in that mass bin. The spacecraft velocities listed in Tab. 1 are always much lower than the dust velocities measured by GIADA. In this condition, in the sun-faced coma (assumed to have uniform space density  $\rho$ ), the dust flux from the nucleus surface corresponds to the dust flux at nadir-pointing GIADA scaled by the factor  $2\pi R^2/A$ . The dust number loss rate at the nucleus surface per GIADA detection is  $Q_n = 2\pi R^2 [A \Delta t]^{-1}$ , where  $\Delta t$  is the total dust collection time (Tabs. 5, 6, 7 and 8). In the same Tables, we show the mass loss rates  $Q_m$  and the mean dust velocities already integrated in each mass bin, corresponding to the four GIADA collection periods considered in this paper: from 19 to 28 February 2015 (Tab. 5), from 13 to 17 March 2015 (Tab. 6), on 28 March 2015 (Tab. 7), and from 23 August to 3 September 2015 (Tab. 8). In Tab. 9 we show the data obtained during the first post-perihelion excursion at low phase angles ( $60 < \alpha < 64$  deg,  $125 < R < 290$  km). The  $R$ -values are too small for using the NAC DUST-MON sequences. The uncertainty affecting  $Af\rho$  and the loss rates measured by GIADA and OSIRIS depends on the number of detections in each mass bin: an esti-

mate of the relative error is given by  $N_p^{-1/2}$  and by  $(N_{gds+is} + N_{is})^{-1/2}$ . The dispersion of the dust velocities in Tabs. 2, 3 and 4 provides the error affecting the dust velocities measured by OSIRIS, close to 30%. The relative error of the dust velocities provided by each GDS+IS detection is below 10%.

### 4. Loss rate of boulders at perihelion

The 67P dust mass distribution at 2.2 au, 2.1 au and perihelion are shown in Figs. 4, 5 and 6, respectively. The dust mass distribution observed by GIADA (smaller mass bins) and OSIRIS (larger mass bins, with a gap of one or two bins in between) are compared to the dust mass distributions from ground-based observations (Fulle et al. 2010). These predictions assumed two values of the dust bulk density ( $10^2 \text{ kg m}^{-3}$  and  $10^3 \text{ kg m}^{-3}$ ) and of the dust geometric albedo ( $A_p = 0.02$  and  $A_p = 0.06$ ). In Figs. 4, 5 and 6, a dust mass distribution constant in all mass bins corresponds to a power law for the differential size distribution with index  $-4$ ; an index  $+1$  in Figs. 4, 5 and 6 corresponds to a differential power index  $= -3$ , and so on. The cut-off at the largest masses observed by OSIRIS in 67P coma agrees with the predictions (Fulle et al. 2010), with a difference of one mass bin before perihelion, and exactly at the predicted average at perihelion. We cannot exclude a bias of the largest detected boulders in the WAC images with respect to NAC images (the S/N of single particles depends on the pixel size in arcsec). The largest possible ejected mass was computed by matching the escape velocity from 67P outer coma ( $0.5 \text{ m s}^{-1}$  at the end of the gas drag) with the dust velocities required to best fit the 67P tail and coma photometry (Fulle et al. 2010). In-situ observations confirm these predictions and show that the highest 67P gas density can lift-up boulders even larger than those observed at  $R > 50$  km. Also, the mechanism determining the cut-off mass of escaping boulders is their fall-back on the nucleus surface where the gas density is lower than at the ejection (e.g., on the nucleus night side).

At 2.2 and 2.1 au inbound, the dust mass distribution observed by OSIRIS matches the predictions of tail models (Fulle et al. 2010). Values smaller than the predictions at the lowest mass bins are affected by large relative errors (small  $N_p$



values in Tabs. 5, 6, 7 and 8). The fact that WAC images can sample the 67P coma closer to the spacecraft than NAC images may introduce a bias also in the largest mass bins. Taking into account these possible biases, at sizes  $> 1$  mm, OSIRIS observations at 2.2 and 2.1 au inbound are consistent with a power index of  $-4$  of the differential size distribution, as required by models of 67P trail (Agarwal et al. 2007), (Agarwal et al. 2010). At perihelion, OSIRIS NAC observations show a clear disagreement with this constraint, which is significant, because 67P trail photometry is mostly sensitive to the dust ejected exactly at perihelion. Using ground-based observations, boulders of mass  $> 1$  kg would not be observable in the trail because they would remain confined in the pixel occupied by the nucleus. Fig. 6 shows that the  $Af\rho$  values at mass  $> 1$  kg give a negligible contribution to the total  $Af\rho$ , even if the ejected mass is strongly dominated by these boulders. We have no observational constraint to exclude that the real dust loss rate of 67P at perihelion is strongly dominated by boulders of mass  $> 1$  kg, with a total dust mass loss rate close to  $2 \times 10^4$  kg s $^{-1}$ , and a dust-to-water mass ratio close to 100. Since this dust-to-water ratio is clearly conflicting with other dust-to-water estimates, e.g. the value of six measured for 67P at 3.6 au inbound (Rotundi et al. 2015), we discuss two possible alternative explanations for the OSIRIS observations of boulders.

The first explanation considers the dust-to-water ratio of the boulders. The largest radius of a boulder that can be lifted from the surface of 67P nucleus ranges from 1 to 3 m (Pajola et al. 2015). The local surface gravity field, the centrifugal force and the drag force produced by the outflowing gas have been taken into account. If these boulders are composed of a significant fraction of water ice, they must be excluded by the dust-to-water ratio computation. In particular, if the dust-to-water mass ratio inside them is even larger than six, they contribute more to the loss rate of water than to the refractory component of 67P. OSIRIS NAC actually provides the opportunity to check this possibility, by means of observations of the same boulder in different filters, observations performed necessarily at different times. This requires considering NAC observations of a resolved boulder, i.e. a boulder covering many

pixels in all useful NAC images. In NAC observations of sub-pixel boulders, it is impossible to disentangle the photometric variations due to the boulder rotation from those really due to the boulder colour. On 30 July 2015, we have detected one boulder which fits all these requirements (Fig. 7). The boulder shape is very irregular. Following the parallax procedure described in Section 2 ( $R = 180$  km), for this boulder we get  $D = 3.5$  km and  $r = 0.4$  m, not far from the model estimates (Pajola et al. 2015). The observed boulder color is bluer than that of the nucleus surface (Tab. 10), with a spectral slope value, evaluated between 480 and 880 nm, of  $-7.5\%$ /(100 nm), while the mean nucleus spectral slope in the same wavelength range is  $+18.1\%$ /(100 nm). Bluer colors across the nucleus are often coupled with higher albedo regions/spots, which have been associated with local maxima of water ice abundance at the nucleus surface (Fornasier et al. 2015), (Pommerol et al. 2015), (Filacchione et al. 2016). This suggests that this boulder has a significant mass fraction of water ice. The spectral slope of dust tracks in the OSIRIS images shows that most of the dust reddening is very similar to the nucleus values, but that a fraction of the dust tracks show negative slopes suggesting a different composition, probably water-ice richer than that of the mean nucleus surface (Cremonese et al. 2016).

The second explanation considers the cloud of boulders in bound orbits observed around 67P nucleus (Rotundi et al. 2015) at 3.6 au inbound. This cloud had dispersed prior to perihelion by the increasing gas outflow, and is replenished at each perihelion passage by a new cloud surviving during the following aphelion (Fulle 1997). Models predict the space density of boulders actually observed in 67P bound cloud (Rotundi et al. 2015). In the mass bin from 10 to 100 kg, 0.12% of the total ejected dust mass during each perihelion passage is injected into bound orbits, with an expected space density of  $7 \times 10^{-12}$  m $^{-3}$ , a value close to that listed in Tab. 8. In the mass bin from 1 to 10 kg, 0.06% of the total ejected dust mass is injected into bound orbits, with an expected space density of  $3 \times 10^{-12}$  m $^{-3}$ . At lower dust masses, the solar radiation pressure prevents any long-lasting stable bound orbit (Richter & Keller 1995). Between the two dust populations, i.e. boulders directly escaping the nucleus gravity

field (only these have to be considered in the computation of the actual 67P dust loss rate), and boulders entering bound orbits around 67P nucleus, there is a third boulder population: boulders entering metastable orbits, i.e. not escaping the nucleus gravity field, but unable to enter orbits stable up to the next aphelion. The number of the boulders in this third population is much larger than that of bound boulders. It is sufficient that 0.06% of the total ejected dust mass from 10 to 100 kg, and 1.8% of mass from 1 to 10 kg, belong to this third boulder population in metastable orbits, in order to explain the observed space density in these mass bins (Tab. 8) at 67P perihelion. We cannot exclude that the real 67P dust loss rate at mass  $> 1$  kg is orders of magnitudes lower than the values shown in Tab. 8 and Fig. 6. If we take into account dust of mass  $< 1$  kg only, the 67P perihelion total dust loss rate is  $(1.5 \pm 0.5) \times 10^3$  kg  $s^{-1}$ .

## 5. Dust-to-water mass ratio

In order to estimate the water loss rate at 2.1 and 2.2 au, we approximate its dependence on the comet heliocentric distance  $r_h$  by a power law of  $r_h$  with an index of -4.6, which provides the observed values of 1.2 kg  $s^{-1}$  at 3.5 au (Rotundi et al. 2015), and of 150 kg  $s^{-1}$  at perihelion (Fulle et al. 2010). We obtain a water loss rate of 13 kg  $s^{-1}$  at 2.1 au, and of 11 kg  $s^{-1}$  at 2.2 au. The dust-to-water mass ratio at the nucleus surface is between five and six at 2.2 au and 2.1 au inbound, and at most ten at perihelion (depending on the percentage of boulders in metastable orbits with respect to those escaping from the nucleus). The 67P dust-to-water mass ratio remains almost constant during the entire inbound orbit. At post-perihelion times, probably most of the dust in mass bins lower than those sampled by GIADA has been ejected (Tab. 9), making it more difficult to estimate the dust-to-water mass ratio in the outbound orbit.

## 6. Time evolution of the dust size distribution

While the uncertainties affecting the 67P dust size distribution extracted from OSIRIS data prevent us from identifying any time evolution at sizes  $> 1$  mm, GIADA data clearly show an evolution

of the 67P dust size distribution at sizes  $< 1$  mm. At 2.2 and 2.1 au inbound, we confirm the results already obtained from 3.6 to 3.4 au inbound. The size distribution is very shallow, with a differential index  $> -2$ . This is confirmed by the  $Af\rho$  quantity, with the same sharp maximum at the size distribution knee already shown between 3.6 and 3.4 au inbound (Rotundi et al. 2015). The  $Af\rho$  quantity integrated over all mass bins is close to the upper limit of the same quantity measured from ground (Fulle et al. 2010). This confirms that the dust size distribution maintains its slope shallower than  $-3$  also at masses  $< 10^{-9}$  kg, with a negligible brightness contribution from smaller dust. The consistency between the dust size distribution and  $Af\rho$  of 67P measured in-situ and from ground indicates that there is no evidence of fragmentation and/or sublimation of compact particles in 67P from  $R \approx 100$  km up to the outermost coma. Fluffy and fragile particles contribute  $< 5\%$  of 67P coma brightness (and much less relative mass) at dust masses  $> 10^{-9}$  kg (Fulle et al. 2015).

At perihelion, the dust size distribution measured by GIADA is much steeper than beyond 2 au, with a differential power index of  $-3.7$ , as predicted (Fulle et al. 2010). This confirms that the low number of detections in the lowest GIADA mass bin beyond 2 au is not due to any instrumental bias, but is due to a real feature of the 67P dust size distribution. This time evolution is confirmed by the  $Af\rho$  quantity, which at perihelion shows a maximum well below the knee of the dust size distribution. The integral of  $Af\rho$  over all mass bins provides a value which is about half of that predicted from ground-based observations (Fulle et al. 2010). About half of 67P coma brightness is provided by dust particles of mass  $< 10^{-9}$  kg, thus confirming that the differential power index remains close to  $-3.6$  in the dust size range from  $0.1 \mu\text{m}$  to 1 mm. The lack of Rosetta orbits favourable to GIADA very close to the spring equinox does not allow us to infer when the 67P dust size distribution actually evolved. Future observations close to 67P autumn equinox (March 2016) will allow us to check if seasons are the drivers for this time evolution. In the outbound orbit, the 67P differential dust size distribution becomes increasingly steeper, with an index  $= -5.7 \pm 2.2$  at  $1.56 < r_h < 1.71$  au (Tab.

9). The large uncertainty in these GIADA data requires further observations before and after the autumn 67P equinox to better constrain this time evolution.

If seasons were responsible for the observed evolution of the dust size distribution at sizes  $< 1$  mm, then this evolution, coupled to the fact that at perihelion the 67P gas density in the sub-solar coma can lift-up meter-size boulders, would suggest that the pristine differential size distribution has a power index between  $-3.6$  and  $-4$  at all sizes, from a few  $\mu\text{m}$  to meters. Dust ejection and fall-back happen mainly during the short perihelion summer, at maximum comet activity. This implies an erosion rate of about 1 m per perihelion in the southern hemi-nucleus (Bertaux 2015), and a fall-back of similar thickness on the northern hemi-nucleus, mainly in night at perihelion. Depending on the nucleus temperature on the night side, part of the gas flux (and of the dust particles dragged in this flow) can fall back on that surface, where the gas re-condenses. On average, dust of size  $> 1$  mm falls back on the nucleus night side without any selection effect, because the 67P night outgassing is too low to affect the trajectories of falling big dust. This explains why, at sizes  $> 1$  mm, both hemi-nuclei have the same size distribution, matching the size distribution observed on the nucleus surface with smooth terrains (Mottola et al. 2015), dominated by dust falling back on the nucleus surface. Dust of size  $< 1$  mm is affected by the low outgassing occurring in 67P night-side at perihelion. The smaller is the falling-back dust, the more effective the repulsion on it by the night outgassing. This explains the knee of the size distribution at a size of about 1 mm, with a depletion of small dust on the hemi-nucleus in winter at perihelion, i.e. a shallower differential index, close to  $-2$  taking into account compact particles only, possibly close to  $-3$  taking into account fluffy particles as well (Fulle et al. 2015).

## 7. Conclusions

Our main results can be summarized as follows:

- The 67P dust environment observed by means of individual dust particle detections by GIADA and OSIRIS instruments on-board Rosetta matches that determined from past ground-based

observations (Fulle et al. 2010). 67P dust size distribution does not change from a nucleus distance of a few hundred km up to the most external coma. The differential dust size distribution is very similar to that directly measured on the 67P nucleus surface for particle larger than a few cm (Mottola et al. 2015). No significant dust fragmentation and/or sublimation occurs in 67P coma.

- 67P dust activity seems to repeat regularly during each orbit. What was observed in-situ in 2015 by Rosetta instruments matches what was extracted from ground-based observations performed before 2010.

- The dust ejection velocities measured in-situ match those extracted by means of coma, tail and trail models (Agarwal et al. 2007), (Agarwal et al. 2010), (Fulle et al. 2010).

- 67P differential dust size distribution at sizes  $> 1$  mm has been extracted by OSIRIS individual particle detections. Although the dust loss rates in this range agree with the predictions based on a power law with index  $-4$ , the bias of WAC detections, and the pollution from boulders in meta-stable and bound orbits do neither allow us to extract a well defined power index, nor to infer any clear time evolution of this index.

- 67P differential dust size distribution at sizes  $< 1$  mm has been extracted from GIADA individual particle detections. We confirm the shallower distribution with respect to the predictions based on past ground-based observations (index  $> -2$  rather than  $-3$ ) beyond 2 au from the Sun (Rotundi et al. 2015). We confirm the strong evolution at perihelion, where an index close to  $-3.7$  has been observed, in agreement with predictions based on ground-based observations (Fulle et al. 2010).

- The mass of the largest boulders observed in-situ matches the predictions of tail models (Fulle et al. 2010). At perihelion, we observe a water-ice rich meter-sized boulder at 3.5 km from the spacecraft, when the gas density at the sub-solar nucleus surface can lift-up even larger boulders (Pajola et al. 2015). The largest ejected mass depends on the fall-back mechanism on 67P nucleus surface where the gas density is much lower (e.g. on the nucleus night side). This mechanism may explain the observed time evolution of the 67P dust size distribution.

– At 67P perihelion, OSIRIS NAC has observed the birth of the 67P cloud of boulders in bound orbits (Fulle 1997), (Rotundi et al. 2015).

– The dust-to-water mass ratio at 67P nucleus surface is close to six during the whole inbound orbit from 3.6 au to perihelion. This value characterizes the nucleus interior too, because the 67P nucleus surface is eroded up to a depth of about 1 m during each perihelion passage (Bertaux 2015).

– Prior to perihelion, both dust mass and coma brightness are dominated by mm-sized particles. After perihelion, both dust mass and coma brightness are dominated by particles of mass  $< 10^{-9}$  kg, so that the Rosetta mission will constrain the dust-to-gas mass ratio with less accuracy than pre-perihelion.

OSIRIS was built by a consortium led by the Max-Planck-Institut für Sonnensystemforschung, Katlenburg-Lindau, Germany, in collaboration with CISAS, University of Padova, Italy, the Laboratoire d’Astrophysique de Marseille, France, the Instituto de Astrofísica de Andalucía, CSIC, Granada, Spain, the Scientific Support Office of the European Space Agency, Noordwijk, The Netherlands, the Instituto Nacional de Técnica Aeroespacial, Madrid, Spain, the Universidad Politécnica de Madrid, Spain, the Department of Physics and Astronomy of Uppsala University, Sweden, and the Institut für Datentechnik und Kommunikationsnetze der Technischen Universität Braunschweig, Germany. The support of the national funding agencies of Germany (DLR), France (CNES), Italy (ASI), Spain (MEC), Sweden (SNSB), and the ESA Technical Directorate is gratefully acknowledged. GIADA was built by a consortium led by the Univ. Napoli Parthenope & INAF–Oss. Astr. Capodimonte, in collaboration with the Inst. de Astrofísica de Andalucía, Selex-ES, FI and SENER. GIADA is presently managed & operated by Ist. di Astrofísica e Planetologia Spaziali-INAf, IT. GIADA was funded and managed by the Agenzia Spaziale Italiana, IT, with the support of the Spanish Ministry of Education and Science MEC, ES. GIADA was developed from a PI proposal from the University of Kent; sci. & tech. contribution were provided by CISAS, IT, Lab. d’Astr. Spat., FR, and Institutions from UK, IT, FR, DE and USA. Science support was provided by NASA through the US Rosetta

Project managed by the Jet Propulsion Laboratory/California Institute of Technology. We would like to thank Angioletta Coradini for her contribution as a GIADA Co-I. GIADA calibrated data will be available through ESAs PSA web site ([www.rssd.esa.int/index.php?project=PSA&page=index](http://www.rssd.esa.int/index.php?project=PSA&page=index)). All data presented here are available on request prior to its archiving in the PSA. We thank the Rosetta Science Ground Segment at ESAC, the Rosetta Mission Operations Center at ESOC and the Rosetta Project at ESTEC for their outstanding work enabling the science return of the Rosetta Mission. This research was supported by the Italian Space Agency (ASI) within the INAF–ASI agreements I/032/05/0 and I/024/12/0.

## REFERENCES

- Agarwal, J., Müller M., Grün E. 2007, *Space Sci. Rev.*, 128, 1-4, 79
- Agarwal, J., Müller M., Reach W.T. et al. 2010, *Icarus*, 207, 992
- Bertaux, J.-L. 2015, *A&A*, 583, A38
- Colangeli, L., Lopez-Moreno J.J., Palumbo P. et al. 2007, *Space Sci. Rev.*, 128, 803
- Cremonese, G., Simioni E., Regazzoni R. et al. 2016, *A&A*, under revision
- Della Corte, V., Rotundi A., Accolla M. et al. 2014, *J. of Astron. Instrumentation*, 3, 1350011–1
- Della Corte, V., Rotundi A., Fulle M. et al. 2015, *A&A*, 583, A13
- Della Corte, V., Sordini R., Accolla M. et al. 2016, *Acta Astronautica*, under review
- Epifani, E., Colangeli L., Fulle M. et al. 2001, *Icarus*, 149, 339
- Ferrari, M., Della Corte V., Rotundi A., et al. 2014, *Plan. & Space Sci.*, 101, 53
- Filacchione, G., De Sanctis M.C., Capaccioni F. et al. 2016, *Nature* (in press)
- Fornasier, S., Hasselmann P.H., Barucci A. et al. 2015, *A&A*, 583, A30
- Fulle, M. 1997, *A&A*, 325, 1237

- Fulle, M. 2004, Comets II, M. C. Festou, H. U. Keller, and H. A. Weaver (eds.), University of Arizona Press, Tucson, p.565
- Fulle, M., Colangeli L., Agarwal J. et al. 2010, A&A, 522, A63
- Fulle, M., Della Corte V., Rotundi A. et al. 2015, ApJ, 802, L12
- Keller, H.U., Barbieri C., Lamy P.L. et al. 2007, Space Sci. Rev., 128, 433
- Mottola, S., Arnold G., Grothues H.-G. et al. 2015, Science, 349, aab0232
- Pajola, M., Vincent J.-B., Güttler C. et al. 2015, A&A, 583, A37
- Pommerol, A., Thomas N., El-Maarry M.R. et al. 2015, A&A, 583, A25
- Richter K., & Keller H.U. 1995, Icarus, 114, 355
- Rotundi, A., Sierks H., Della Corte V. et al. 2015, Science, 347, aaa3905
- Sekanina, Z. 1988, AJ, 95, 911
- Thomas, N., Davidsson B., El-Maarry M.R. et al. 2015, A&A, 583, A17

TABLE 1  
GEOMETRY OF OSIRIS OBSERVATIONS

Date UT <sup>a</sup>	$r_h$ <sup>b</sup>	$R$ <sup>c</sup>	$\alpha$ <sup>d</sup>	$v_{sc}$ <sup>e</sup>	$v_{scz}$ <sup>f</sup>	$\delta$ <sup>g</sup>
28/02/15	2.20	110	63	0.27	0.24	30
14/03/15	2.10	80	52	0.27	0.21	30
27/08/15	1.25	400	79	1.09	0.10	23

<sup>a</sup>dd/mm/yy

<sup>b</sup>heliocentric distance (au)

<sup>c</sup>nucleus-spacecraft distance (km)

<sup>d</sup>phase angle (deg)

<sup>e</sup>sky-projected spacecraft velocity ( $\text{m s}^{-1}$ )

<sup>f</sup>spacecraft velocity projected along the line of sight ( $\text{m s}^{-1}$ )

<sup>g</sup>counter-clock-wise angle between the OSIRIS horizontal image axis and the spacecraft velocity projected on the sky (deg)

TABLE 2  
 PHOTOMETRIC AND GEOMETRIC DATA OF THE 28 SINGLE DETECTIONS IN THE 8 WAC PAIRS OF IMAGES  
 OF SEQUENCE STP045–DUST–MON003 COLLECTED ON 28 FEBRUARY 2015

$N$	$I$ <sup>a</sup>	$a$ <sup>b</sup>	$b$ <sup>c</sup>	$r$ <sup>d</sup>	$m$ <sup>e</sup>	$\gamma$ <sup>f</sup>	$\beta$ <sup>g</sup>	$v$ <sup>h</sup>
01	4.2	14.3	21	2.4	5.8E-05	4.2	-27	1.9
02	10.0	5.4	50	8.9	3.0E-03	1.6	-3	0.5
03	1.9	2.7	100	7.8	2.0E-03	0.9	+3	0.9
04	2.4	6.4	43	3.8	2.3E-04	1.6	+7	1.2
05	5.3	2.8	98	12.7	8.6E-03	3.5	+9	0.7
06	1.4	2.7	111	7.4	1.7E-03	6.0	-26	1.3
07	10.1	17.9	15	2.7	8.2E-05	–	0	–
08	3.7	3.2	96	10.4	4.7E-03	3.4	+29	2.5
09	3.7	11.1	24	2.6	7.4E-05	1.1	+6	1.5
10	5.4	3.5	81	10.6	5.0E-03	5.5	+18	0.9
11	1.8	2.8	106	8.1	2.2E-03	2.1	+25	3.4
12	5.0	10.2	33	4.2	3.1E-04	2.0	+36	5.6
13	1.0	2.7	104	5.9	8.6E-04	5.2	+15	0.8
14	0.7	1.7	185	8.7	2.8E-03	5.5	+31	1.7
15	3.5	3.0	91	9.6	3.7E-03	–	+10	–
16	5.5	51.2	5	0.7	1.4E-06	1.0	-8	2.2
17	4.6	3.4	80	9.7	3.8E-03	3.6	-8	0.6
18	4.5	4.7	59	7.1	1.5E-03	2.4	+14	1.6
19	2.7	6.4	44	4.1	2.9E-04	1.1	+15	3.8
20	1.7	4.2	72	5.3	6.2E-04	4.2	+27	1.9
21	3.7	1.7	162	17.6	2.3E-02	3.6	+11	0.8
22	3.3	4.1	67	6.8	1.3E-03	–	+11	–
23	2.3	2.3	118	10.1	4.3E-03	1.4	-6	1.2
24	1.6	0.7	399	28.5	9.7E-02	–	+15	–
25	1.0	0.8	338	19.1	2.9E-02	1.2	-3	0.7
26	8.4	7.7	35	5.7	7.8E-04	0.3	-1	0.8
27	5.6	16.7	16	2.1	3.9E-05	–	+1	–
28	1.4	2.4	113	7.5	1.8E-03	3.7	-2	0.2

<sup>a</sup>integrated particle brightness in percentage of nucleus surface brightness (the nucleus is in the center of all 16 images)

<sup>b</sup>sky-projected speed of the dust particle (px s<sup>-1</sup>)

<sup>c</sup>WAC pixel size at the particle distance  $D$  from the spacecraft,  $D = 10^4 b$  (mm)

<sup>d</sup>particle radius, assuming that the particle and the nucleus have the same albedo times the phase function (mm)

<sup>e</sup>particle mass, assuming a bulk density of 10<sup>3</sup> kg m<sup>-3</sup> (kg)

<sup>f</sup>sky-projected angle between the nucleus and the particle trajectory across the full image (deg)

<sup>g</sup>counter-clock-wise angle between the sky-projected spacecraft velocity  $v_{sc}$  and the apparent particle velocity (deg)

<sup>h</sup>particle radial speed from the nucleus.  $v$  cannot be computed if the particle has an apparent motion converging to the nucleus ( $\text{m s}^{-1}$ )



TABLE 3

PHOTOMETRIC AND GEOMETRIC DATA OF THE 74 SINGLE DETECTIONS IN THE 9 WAC PAIRS OF IMAGES OF SEQUENCE STP049–DUST–MON001 COLLECTED ON 14 MARCH 2015. SEE TAB. 2 FOR EXPLANATIONS

$N$	$I$	$a$	$b$	$r$	$m$	$\gamma$	$\beta$	$v$
01	1900	defocus	0.48	1.2	6.9E-06	–	–	–
02	11.9	8.1	34	6.7	1.2E-03	–	10	–
03	6.4	25.5	18	2.6	7.3E-05	3.1	54	4.0
04	28.6	7.9	44	13.3	9.9E-03	6.0	40	1.7
05	1.7	3.1	105	7.7	1.9E-03	6.7	31	1.2
06	4.0	13.1	23	2.6	7.7E-05	4.5	26	1.5
07	1.0	2.8	90	5.1	5.6E-04	-2.8	5	0.5
08	3.5	10.1	30	3.2	1.4E-04	1.3	27	5.4
09	1.7	11.2	41	3.0	1.2E-04	4.0	54	3.2
10	1.8	6.8	39	2.9	1.1E-04	–	8	–
11	3.3	10.2	27	2.8	9.3E-05	1.2	10	2.2
12	41.5	11.0	28	10.2	4.4E-03	5.1	29	1.5
13	1.8	10.8	27	2.0	3.4E-05	-3.0	22	1.9
14	2.8	7.0	39	3.7	2.1E-04	-1.7	7	1.1
15	1.9	4.1	67	5.2	6.1E-04	–	0	–
16	1.0	3.0	91	5.1	5.7E-04	0.5	9	4.5
17	2.4	5.2	55	4.8	4.6E-04	–	10	–
18	2.4	2.0	137	12.0	7.2E-03	–	9	–
19	2.8	1.8	139	13.1	9.5E-03	–	14	–
20	3.1	12.7	22	2.1	4.1E-05	0.9	15	4.5
21	1.3	1.9	140	9.0	3.1E-03	1.4	16	3.0
22	4.5	3.0	94	11.2	5.9E-03	3.4	16	1.2
23	4.3	4.1	68	8.0	2.1E-03	-4.1	7	0.5
24	3.9	2.0	139	15.5	1.6E-02	–	14	–
25	2.0	3.2	90	7.2	1.6E-03	–	0	–
26	2.9	2.9	95	9.1	3.2E-03	1.5	18	3.2
27	2.3	4.2	68	5.8	8.3E-04	0.3	7	7.4
28	1.0	2.1	139	7.9	2.0E-03	1.9	14	2.0
29	3.4	6.8	42	4.3	3.4E-04	-6.8	23	0.9
30	5.2	6.2	45	5.8	8.2E-04	–	4	–
31	10.9	7.1	40	7.5	1.7E-03	–	16	–
32	2.6	3.1	91	8.3	2.4E-03	–	9	–
33	3.4	3.9	67	7.0	1.5E-03	–	0	–
34	10.0	7.1	39	6.9	1.4E-03	2.0	8	1.1
35	5.1	25.8	11	1.4	1.2E-05	3.6	22	1.6
36	2.4	1.1	285	24.9	6.4E-02	4.0	18	1.2
37	1.5	2.2	151	10.4	4.8E-03	–	27	–
38	1.5	1.0	278	19.2	3.0E-02	-1.7	14	2.2
39	2.7	2.9	93	8.6	2.7E-03	-2.3	14	1.6
40	4.1	1.0	272	31.1	1.3E-02	0.1	8	18.9
41	0.6	1.9	139	6.1	9.4E-04	–	14	–

TABLE 3—*Continued*

$N$	$I$	$a$	$b$	$r$	$m$	$\gamma$	$\beta$	$v$
42	0.5	1.8	135	5.4	6.5E-04	–	0	–
43	5.2	10.7	25	3.2	1.3E-04	-2.8	3	0.3
44	2.6	6.2	45	4.1	2.9E-04	-0.8	4	1.4
45	3.0	3.9	73	7.2	1.5E-03	3.0	23	2.0
46	3.6	2.2	139	14.9	1.4E-02	1.3	14	2.9
47	1.3	4.1	70	4.5	3.9E-04	2.8	16	1.5
48	5.4	3.9	70	9.1	3.2E-03	–	14	–
49	6.6	24.7	14	2.0	3.2E-05	-7.6	37	1.2
50	2.7	3.8	73	6.8	1.3E-03	–	23	–
51	2.4	2.1	138	12.0	7.3E-03	–	11	–
52	2.9	4.2	70	6.8	1.3E-03	–	17	–
53	1.4	7.9	37	2.5	6.4E-05	3.0	25	2.2
54	1.8	3.8	68	5.2	5.8E-04	-3.2	8	0.7
55	2.5	9.8	27	2.4	5.9E-05	-1.1	5	1.2
56	9.3	21.7	13	2.2	4.2E-05	-4.2	12	0.8
57	4.1	6.8	39	4.4	3.7E-04	-1.8	8	1.2
58	2.6	7.9	36	3.2	1.4E-04	–	18	–
59	1.4	3.9	68	4.5	3.8E-04	–	0	–
60	6.8	8.8	32	4.8	4.6E-04	3.6	22	1.6
61	0.3	5.9	45	1.4	1.1E-05	–	0	–
62	2.8	12.1	23	2.1	4.1E-05	0.6	5	2.3
63	2.1	4.1	70	5.7	7.7E-04	–	14	–
64	1.5	3.9	70	4.8	4.7E-04	-5.9	14	0.6
65	6.2	4.8	55	7.7	1.9E-03	-6.2	11	0.5
66	18.6	13.8	20	4.8	4.7E-04	-3.8	14	1.0
67	2.2	6.2	47	3.9	2.5E-04	-6.0	15	0.7
68	3.5	2.0	151	15.9	1.7E-02	–	27	–
69	1.5	4.1	68	4.7	4.3E-04	–	0	–
70	3.3	2.9	95	9.7	3.9E-03	1.0	18	4.8
71	1.4	2.1	13	9.2	3.2E-03	1.2	11	2.5
72	3.2	4.9	54	5.5	6.9E-04	2.4	7	0.8
73	1.2	1.8	139	8.6	2.7E-03	6.5	14	0.6
74	0.6	0.8	382	16.7	1.9E-02	-2.0	45	5.4

TABLE 4

PHOTOMETRIC AND GEOMETRIC DATA OF THE 102 SINGLE DETECTIONS IN THE 8 NAC PAIRS OF IMAGES OF SEQUENCE STP071-DUST-MON001 COLLECTED ON 27 AUGUST 2015. SEE TAB. 2 FOR EXPLANATIONS

$N$	$I$ <sup>a</sup>	$a$	$b$ <sup>b</sup>	$r$	$m$	$\gamma$	$\beta$	$v$
001	3.9	1.3	978	109	5.4E-00		29	
003	1.0	1.7	630	35	1.8E-01		4	
010	3.6	2.1	620	66	1.2E-00		33	
011	2.7	7.1	206	19	2.9E-02		43	
012	1.6	3.6	299	21	3.9E-02		2	
013	1.5	2.3	465	32	1.4E-01		1	
016	1.4	2.1	530	35	1.8E-01		11	
017	9.5	1.6	665	115	6.4E-00		-5	
018	7.7	1.8	640	100	4.2E-00		22	
019	1.8	1.8	595	45	3.8E-01		-5	
020	8.8	7.2	167	28	9.2E-02		27	
025	6.2	9.2	117	16	1.7E-02	0.4	3	7.7
026	1.8	2.7	428	32	1.4E-01		22	
030	0.3	6.4	175	5	6.6E-04		16	
031	6.6	2.1	657	95	3.6E-00		40	
034	53.0	9.5	145	59	8.6E-01		38	
042	92.6	14.6	74	40	2.7E-01		4	
043	5.2	1.5	753	97	3.8E-00		17	
045	10.5	1.7	630	115	6.4E-00		4	
048	4.4	1.6	658	78	2.0E-00	0.3	-2	7.6
052	3.2	1.7	652	66	1.2E-00		18	
054	6.5	2.5	475	68	1.3E-00		23	
055	> 100	10.7	106	200	3.3E+01		18	
056	3.7	1.5	873	95	3.6E-00		37	
059	3.7	1.5	702	76	1.8E-00	0.6	7	11.8
060	7.2	2.2	564	85	2.6E-00		29	
063	16.5	5.6	211	48	4.6E-01		23	
067	4.8	2.0	589	73	1.6E-00		26	
071	2.5	3.4	315	28	9.2E-02	0.9	4	5.1
073	3.6	2.2	506	54	6.6E-01	1.0	13	14.8
074	3.6	1.5	808	87	2.8E-00		27	
076	4.4	3.1	367	43	3.3E-01		20	
077	6.9	6.4	188	28	9.2E-02		26	
082	14.1	2.4	477	101	4.3E-00		22	
086	8.6	4.1	271	45	3.8E-01		14	
088	2.0	2.5	497	40	2.7E-01		28	
094	4.7	2.6	442	54	6.6E-00		19	
097	4.0	2.1	657	74	1.7E-00		40	
101	28.3	4.4	401	120	7.2E-00		52	
102	11.6	3.4	397	76	1.8E-00		36	
103	11.1	13.2	83	15	1.4E-02		-8	

TABLE 4—*Continued*

$N$	$I$ <sup>a</sup>	$a$	$b$ <sup>b</sup>	$r$	$m$	$\gamma$	$\beta$	$v$
105	4.9	3.8	285	36	2.0E-01	0.7	1	1.6
106	3.9	4.1	286	32	1.4E-01	1.0	22	23.8
107	2.8	2.9	373	35	1.8E-01	1.0	9	9.2
108	10.6	1.5	701	129	8.8E-00		6	
112	13.0	1.7	628	128	8.8E-00		3	
114	13.1	2.0	556	114	6.2E-00		18	
115	11.0	2.9	433	81	2.2E-00		30	
118	3.8	2.3	471	52	5.6E-01	0.5	12	23.6
119	3.4	3.4	320	33	1.5E-01	0.5	1	2.2
120	21.2	3.3	336	87	2.8E-00	0.6	13	24.0
121	2.0	1.8	679	54	6.6E-03		26	
123	28.6	3.2	343	104	4.7E-00	0.7	10	15.0
125	47.4	6.1	228	88	2.9E-00		39	
128	3.7	3.8	287	31	1.2E-01	0.7	7	10.1
134	1.6	2.0	549	39	2.5E-01	0.7	6	9.1
139	> 100	24.1	45	135	1.0E+01		2	
143	32.6	2.6	420	135	1.0E+01		4	
150	1.7	2.3	451	33	1.6E-01		12	
154	6.1	3.8	285	40	2.7E-01	0.9	1	1.2
157	4.9	10.2	107	13	9.2E-03	1.0	6	6.8
159	3.8	4.4	247	27	8.2E-02	0.9	6	7.6
162	2.4	1.6	670	59	8.6E-01		13	
165	4.3	2.3	465	54	6.6E-01		1	
166	77.8	1.9	579	288	1.0E+02		14	
168	2.8	2.8	382	36	2.0E-01		5	
176	11.5	1.9	781	149	1.4E+01		43	
178	7.8	3.9	284	45	3.8E-01		15	
179	59.0	7.2	150	65	1.2E-00	0.2	2	13.6
182	1.4	2.3	471	31	1.2E-01	0.8	12	16.3
189	7.0	2.2	564	84	2.5E-00		29	
192	3.3	1.9	649	67	1.3E-00		30	
193	5.3	1.2	923	120	7.2E+01		18	
194	9.7	7.1	158	28	8.2E-01		16	
195	16.7	16.0	68	16	1.7E-02		10	
198	82.3	6.3	189	94	3.5E-00		24	
200	15.1	12.7	104	23	5.1E-02		35	
202	1.0	17.0	80	5	3.8E-04		22	
203	12.2	16.2	69	13	9.2E-03		13	
204	7.2	18.1	61	9	3.2E-03		10	
205	6.1	1.6	762	106	5.0E-00		31	
206	9.2	11.7	92	16	1.7E-02	0.3	2	6.4

TABLE 4—*Continued*

$N$	$I$ <sup>a</sup>	$a$	$b$ <sup>b</sup>	$r$	$m$	$\gamma$	$\beta$	$v$
209	5.7	22.9	670	90	3.1E-00		13	
215	17.9	22.9	48	11	5.6E-03	0.7	10	15.7
219	4.3	5.8	193	23	4.5E-02	0.5	14	27.4
220	6.8	1.5	702	103	4.6E-00	0.9	7	8.6
221	4.8	5.2	216	27	7.4E-02	0.9	16	18.6
229	7.7	1.9	579	91	3.1E-00	1.0	14	14.4
230	1.6	3.1	352	25	6.5E-01	0.7	7	9.9
232	2.1	2.2	465	38	2.3E-01	0.9	1	1.1
233	11.3	6.3	172	33	1.5E-01		0	
234	2.7	2.7	428	40	2.7E-01		22	
235	9.2	2.3	515	88	2.9E-00		25	
237	7.9	3.0	389	62	1.0E-00		22	
241	13.8	2.7	412	86	2.7E-00		16	
243	3.9	1.9	649	72	1.6E-00		30	
245	0.6	5.2	216	9	3.2E-03		16	
247	3.4	4.6	236	25	6.5E-02		-1	
248	5.5	4.6	257	34	1.6E-01		25	
250	4.4	9.4	122	14	1.1E-02		20	
253	7.6	8.4	160	25	6.5E-02		37	
254	11.9	1.7	630	122	7.6E-00	0.9	4	4.9

<sup>a</sup>When  $I > 100\%$  the particle radius was directly measured in the NAC image

<sup>b</sup>The particle distance from the spacecraft is  $D = 5.4 \times 10^4 b$ . Only particles with  $D < 50$  km have been taken into account

TABLE 5  
DUST SIZE DISTRIBUTION OF 67P AT 2.2 AU PRE-PERHELION

$\Delta m$	<sup>a</sup> $N_p/N_i$	<sup>b</sup> $N_{gds+is}$	<sup>c</sup> $N_{is}$	<sup>d</sup> $D$	<sup>e</sup> $\rho$	<sup>f</sup> $v$	<sup>g</sup> $Q_n$	<sup>h</sup> $Q_m$	<sup>i</sup> $\sigma$	<sup>j</sup> $Af\rho$	<sup>k</sup>
1E-02–1E-01	3/8	–	–	3.99	4.4E-10	0.6	2.0E+01	1.0	1.6E-03	6.9E-03	
1E-03–1E-02	14/8	–	–	1.85	2.1E-08	1.1	1.8E+03	5.9	2.7E-04	5.7E-02	
1E-04–1E-03	6/8	–	–	1.04	5.0E-08	2.1	8.0E+03	4.1	7.7E-05	3.8E-02	
1E-05–1E-04	4/8	–	–	0.24	2.7E-06	1.5	3.1E+05	19.5	1.9E-05	5.1E-01	
1E-06–1E-05	1/8	–	–	0.05	7.5E-05	2.2	1.1E+07	15.4	1.5E-06	1.1E-00	
1E-07–1E-06	–	–	–	–	–	–	–	–	–	–	
1E-08–1E-07	–	14	13	–	–	5.5	1.1E+08	5.24	1.6E-07	4.2E-01	
1E-09–1E-08	–	0	2	–	–	15.	1.1E+07	0.06	3.8E-08	3.6E-03	

<sup>a</sup>mass bins (kg). 5 upper mass bins: data from 28 OSIRIS single particle detections on 28 February 2015 (Tab. 2), assumed dust bulk density of  $10^3 \text{ kg m}^{-3}$ . 2 lower mass bins: 29 GIADA single particle detections from 19 to 28 February 2015 ( $\Delta t = 7.3 \times 10^5 \text{ s}$ )

<sup>b</sup>number of OSIRIS detections  $N_p$  averaged over the number of different images  $N_i$

<sup>c</sup>number of GIADA detections by the GDS and IS sensors (measurement of dust mass and velocity)

<sup>d</sup>number of GIADA detections by the IS sensor only, dust velocity assumed from tail model (Fulle et al. 2010)

<sup>e</sup>the largest distance from the spacecraft at which a particle has been detected (km)

<sup>f</sup>dust space density, provided by  $N$  divided by the sampled coma volume up to the distance  $D$  ( $\text{m}^{-3}$ )

<sup>g</sup>measured dust radial velocity (assumed (Fulle et al. 2010) if  $N_{gds+is} = 0$ ) ( $\text{m s}^{-1}$ )

<sup>h</sup>dust number loss rates at the nucleus surface ( $\text{s}^{-1}$ )

<sup>i</sup>dust mass loss rates at the nucleus surface ( $\text{kg s}^{-1}$ )

<sup>j</sup>dust cross section ( $\text{m}^2$ )

<sup>k</sup>dust coma brightness, see text for explanation (m)

TABLE 6  
DUST SIZE DISTRIBUTION OF 67P AT 2.1 AU PRE-PERHELION (SEE TAB. 5 FOR EXPLANATIONS)

$\Delta m$	<sup>a</sup> $N_p/N_i$	$N_{gds+is}$	$N_{is}$	$D$	$\rho$	$v$	$Q_n$	$Q_m$	$\sigma$	$Af\rho$
1E-02–1E-01	7/9	–	–	3.82	1.0E-09	2.7	1.1E+02	2.8	1.0E-03	5.3E-03
1E-03–1E-02	27/9	–	–	1.51	6.5E-08	1.6	4.2E+03	13.4	2.6E-04	8.8E-02
1E-04–1E-03	27/9	–	–	1.39	8.4E-08	1.7	5.7E+03	2.6	7.1E-05	3.1E-02
1E-05–1E-04	13/9	–	–	0.45	1.2E-06	1.9	9.2E+04	4.1	1.5E-05	9.5E-02
1E-06–1E-05	–	–	–	–	–	–	–	–	–	–
1E-07–1E-06	–	7	0	–	–	0.5	1.7E+07	7.66	7.0E-07	3.1E+00
1E-08–1E-07	–	5	19	–	–	9.1	7.9E+07	1.66	9.3E-08	1.1E-01
1E-09–1E-08	–	0	7	–	–	15.	4.4E+07	0.18	3.0E-08	1.1E-02

<sup>a</sup>4 upper mass bins: data from 74 OSIRIS single particle detections on 14 March 2015 (Tab. 3, assumed dust bulk density of  $10^3 \text{ kg m}^{-3}$ ). 3 lower mass bins: 38 GIADA single particle detections on 28 March 2015 ( $\Delta t = 6.5 \times 10^4 \text{ s}$ )

TABLE 7

DUST SIZE DISTRIBUTION OF 67P AT 2.1 AU PRE-PERHELION (SEE TAB. 5 FOR EXPLANATIONS)

$\Delta m$	<sup>a</sup> $N_p/N_i$	$N_{gds+is}$	$N_{is}$	$D$	$\rho$	$v$	$Q_n$	$Q_m$	$\sigma$	$Af\rho$
1E-02–1E-01	15/9	–	–	3.82	2.2E-09	2.6	2.3E+02	10.4	1.5E-03	1.7E-02
1E-03–1E-02	38/9	–	–	1.40	1.2E-07	1.6	7.7E+03	30.8	3.0E-04	1.8E-01
1E-04–1E-03	17/9	–	–	0.47	1.4E-06	2.0	1.1E+05	37.4	5.9E-05	4.2E-01
1E-05–1E-04	4/9	–	–	0.45	3.7E-07	1.2	1.8E+04	0.85	1.6E-05	3.1E-02
1E-06–1E-05	–	–	–	–	–	–	–	–	–	–
1E-07–1E-06	–	1	1	–	–	3.5	2.0E+07	4.3	2.1E-07	1.6E-01
1E-08–1E-07	–	17	52	–	–	9.3	7.0E+08	18.9	5.2E-08	5.1E-01
1E-09–1E-08	–	2	8	–	–	14.5	1.0E+08	0.37	1.4E-08	1.3E-02

<sup>a</sup>4 upper mass bins: data from 74 OSIRIS single particle detections on 14 March 2015 (Tabs. 3, assumed dust bulk density of  $3 \times 10^3 \text{ kg m}^{-3}$ ). 3 lower mass bins: 81 GIADA single particle detections from 13 to 17 March 2015 ( $\Delta t = 4.1 \times 10^5 \text{ s}$ )



TABLE 8  
DUST SIZE DISTRIBUTION OF 67P AT PERIHELION (SEE TAB. 5 FOR EXPLANATIONS)

$\Delta m$	<sup>a</sup> $N_p/N_i$	$N_{gds+is}$	$N_{is}$	$D$	$\rho$	$v$	$Q_n$	$Q_m$	$\sigma$	$Af\rho$
1E+01–1E+02	5/8	–	–	50	1.0E-11	8.2	8.2E+01	3.0E+03	1.3E-01	0.16
1E-00–1E+01	39/8	–	–	49	8.8E-11	14.0	1.2E+03	4.0E+03	2.7E-02	0.30
1E-01–1E-00	33/8	–	–	34	2.2E-10	10.3	2.3E+03	8.1E+02	6.0E-03	0.17
1E-02–1E-01	18/8	–	–	19	6.9E-10	10.8	7.5E+03	3.5E+02	1.6E-03	0.14
1E-03–1E-02	5/8	–	–	11	9.9E-10	12.8	1.3E+04	7.9E+01	4.0E-04	0.05
1E-04–1E-03	2/8	–	–	9	7.2E-10	16.0	1.2E+04	4.8E+00	6.6E-05	0.01
1E-05–1E-04	–	–	–	–	–	–	–	–	–	–
1E-06–1E-05	–	–	–	–	–	–	–	–	–	–
1E-07–1E-06	–	2	0	–	6.9E-06	26	1.8E+08	7.6E+01	6.8E-07	0.61
1E-08–1E-07	–	5	24	–	1.2E-04	20	2.5E+09	5.3E+01	9.2E-08	1.50
1E-09–1E-08	–	1	92	–	2.4E-04	35	8.4E+09	5.1E+01	4.0E-08	1.25

<sup>a</sup>6 upper mass bins: data from 102 OSIRIS single particle detections on 27 August 2015 (Tab. 4, assumed dust bulk density of  $10^3 \text{ kg m}^{-3}$ ). 3 lower mass bins: 124 GIADA single particle detections from 23 August to 3 September 2015 ( $\Delta t = 1.1 \times 10^6 \text{ s}$ )

TABLE 9  
DUST SIZE DISTRIBUTION OF 67P AT  $1.56 < r_h < 1.71$  AU POST-PERHELION (SEE TAB. 5 FOR EXPLANATIONS)

$\Delta m$	<sup>a</sup> $N_{gds+is}$	$N_{is}$	$v$	$Q_m$
1E-06–1E-05	1	0	15	1.3
1E-07–1E-06	0	2	10	0.8
1E-08–1E-07	3	101	10	9.13
1E-09–1E-08	1	15	6	0.14

<sup>a</sup>mass bins (kg). 123 GIADA single particle detections from 1 to 20 November 2015 ( $\Delta t = 1.8 \times 10^6$  s)

TABLE 10  
 PHOTOMETRY OF THE RESOLVED BOULDER SHOWN IN FIG. 7

Time UT <sup>a</sup>	$\lambda$ <sup>b</sup>	$(I/F)_N$ <sup>c</sup>	$(I/F)_B$ <sup>d</sup>
22h07m13s	481	1.26E-03	5.81E-03
22h07m02s	882	4.06E-03	2.18E-03

<sup>a</sup>Observation time of the boulder on 30 July 2015

<sup>b</sup>central wavelength of OSIRIS NAC filter (nm)

<sup>c</sup>fraction of solar light flux scattered by the nucleus at  $\alpha = 90$  deg

<sup>d</sup>fraction of solar light flux scattered by the boulder at  $\alpha = 90$  deg

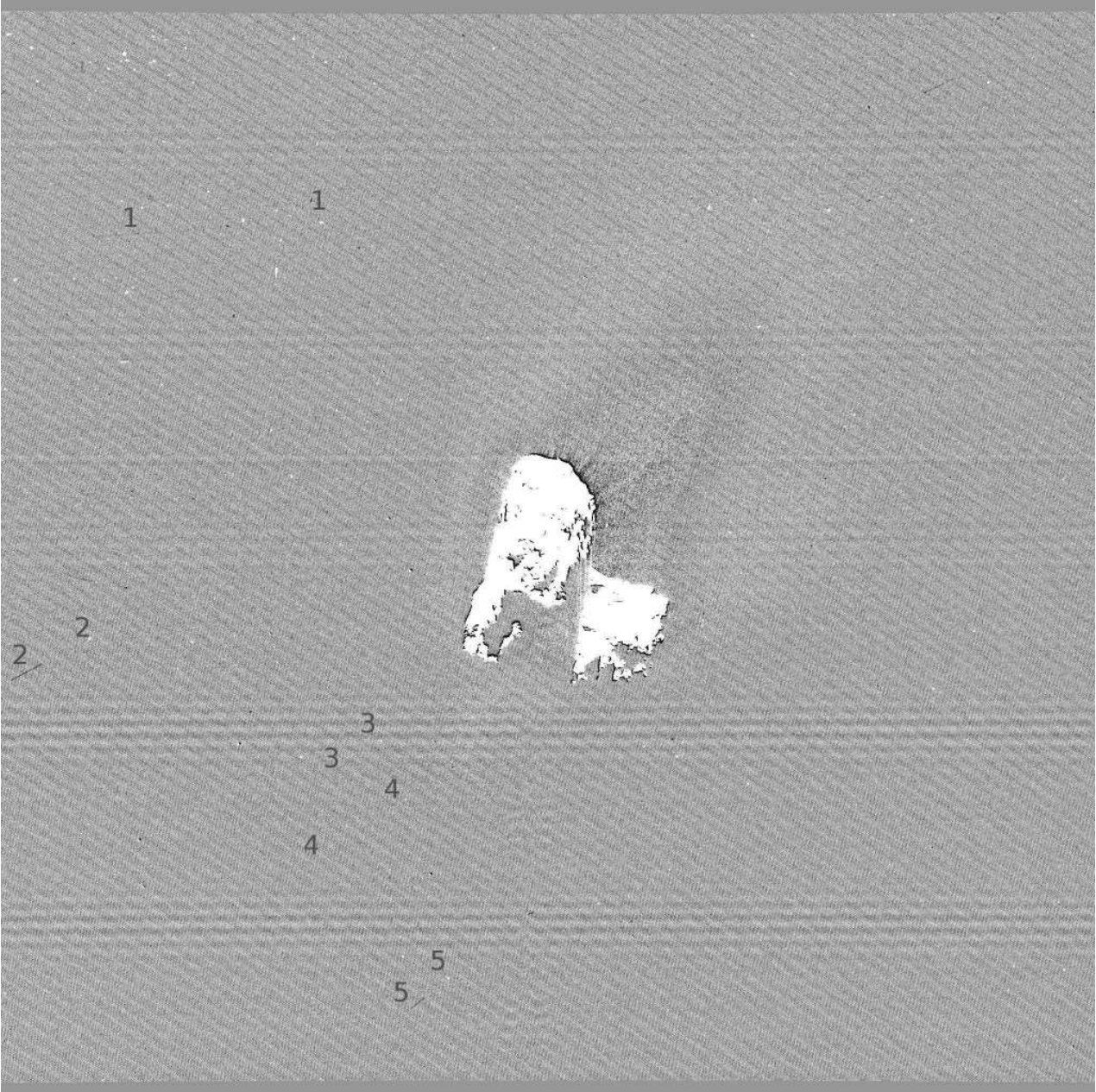


Fig. 1.— OSIRIS WAC subtraction image between the exposures of 0.48 and 12 sec taken on 28 February 2015, 11h35m UT. The numbers mark the first 5 identified moving dust particles of the sequence STP045–DUST–MON003 (Tab. 2). 67P nucleus at image center.

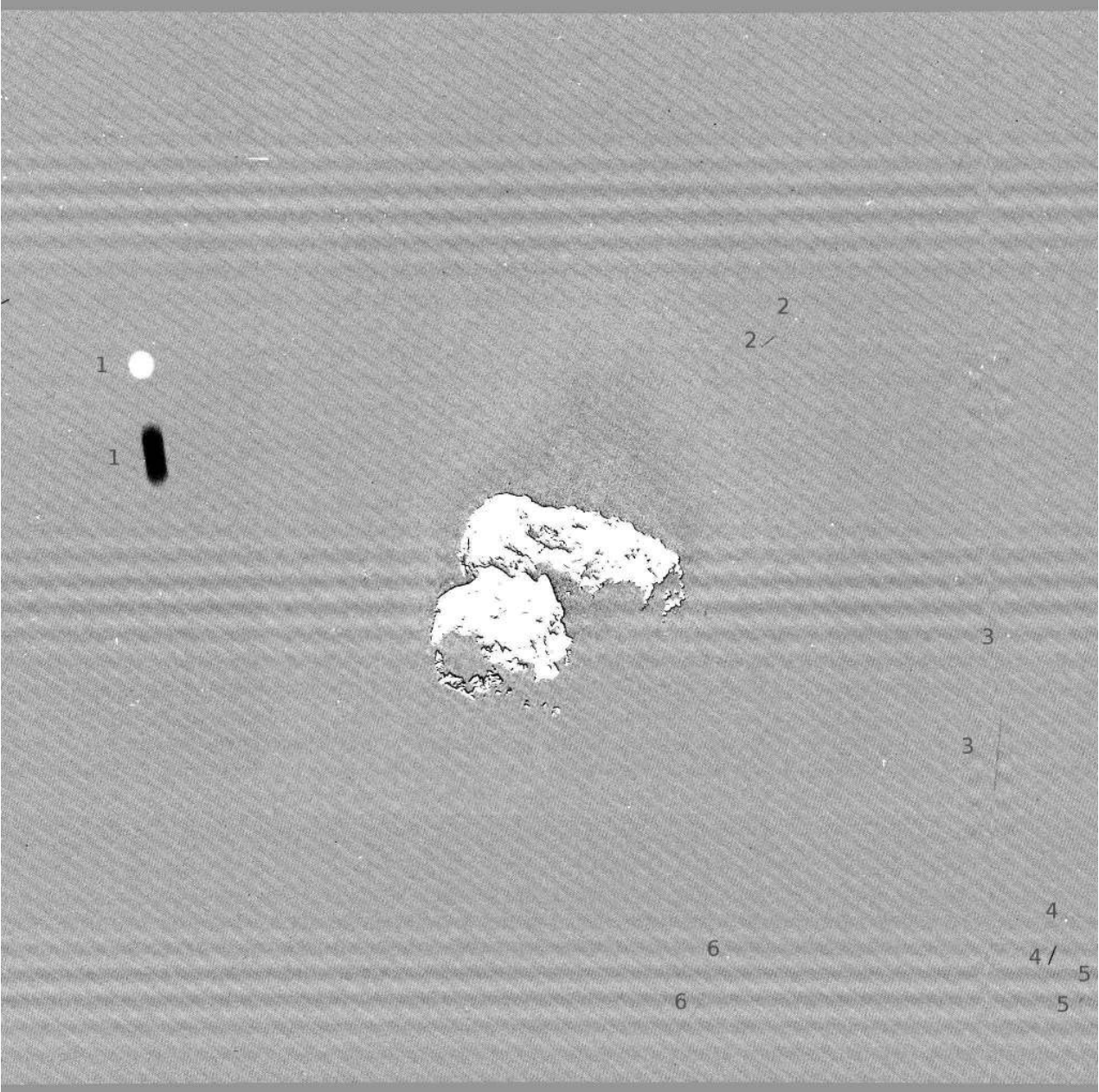


Fig. 2.— OSIRIS WAC subtraction image between the exposures of 0.24 and 6 sec taken on 14 March 2015, 02h37m UT. The numbers mark the first 6 identified moving dust particles of the sequence STP049–DUST–MON001, see Tab. 3 for the full data set. The track 1 is out of focus, its size has directly provided the particle distance.

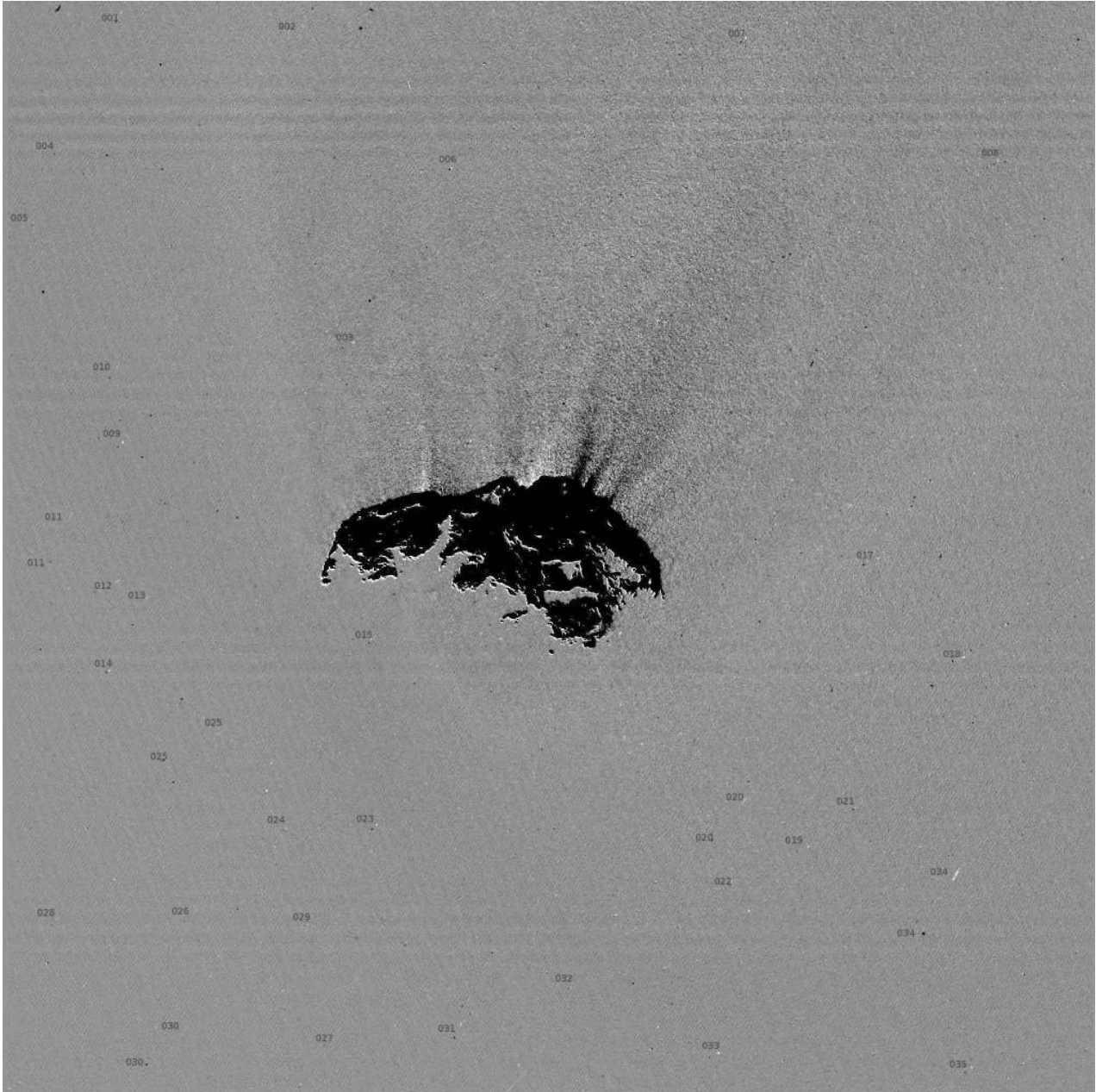


Fig. 3.— OSIRIS NAC subtraction image between the exposures of 2.4 and 0.096 sec taken on 27 August 2015, 05h51m UT. The numbers mark the first 35 identified moving dust particles of the sequence STP071–DUST–MON001, see Tab. 4 for the full data set.

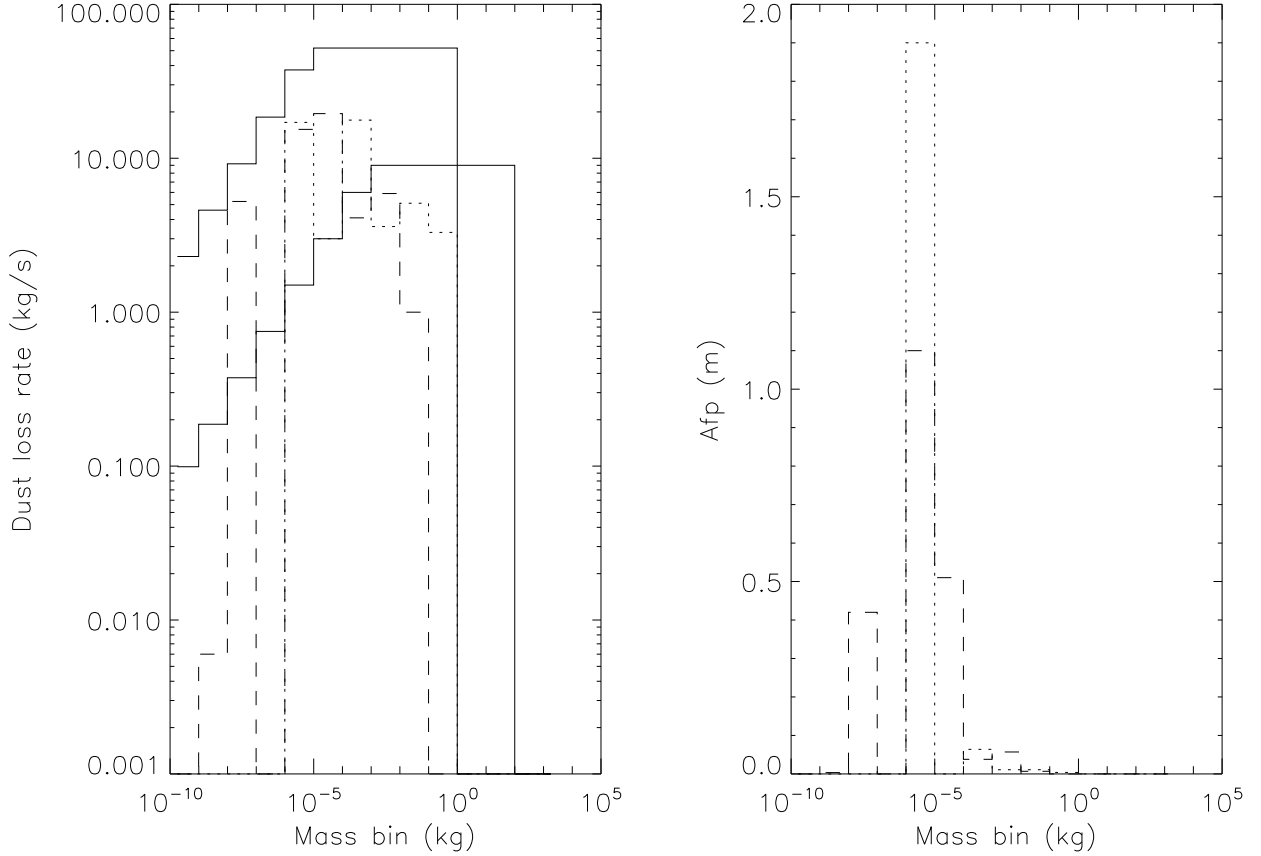


Fig. 4.— 67P dust mass distribution at 2.2 au pre-perihelion. Left panel, continuous line: upper and lower limits of the predicted dust loss rate (Fulle et al. 2010). The power index of the associated differential size distribution is  $-3$  below  $10^{-6}$  kg and  $-4$  above  $10^{-5}$  kg. Left panel, dashed line: observed dust loss rate (29 GIADA detections in the 2 lower mass bins; and 28 OSIRIS detections in the 5 upper mass bins, assumed bulk density of  $10^3$  kg m $^{-3}$ ; data in Tab. 5). Left panel, dotted line: observed dust loss rate (28 OSIRIS detections in the 5 upper mass bins, assumed bulk density of  $3 \times 10^3$  kg m $^{-3}$ ). Right panel: observed  $Af\rho$  (GIADA detections in the 2 lower mass bins, OSIRIS detections in the 5 upper mass bins; dashed line, assumed dust bulk density of  $10^3$  kg m $^{-3}$ ; dotted line, assumed dust bulk density of  $3 \times 10^3$  kg m $^{-3}$ ). The total dust loss rate is  $60 \pm 10$  kg s $^{-1}$ . The total  $Af\rho$  is  $2.2 \pm 0.2$  m.

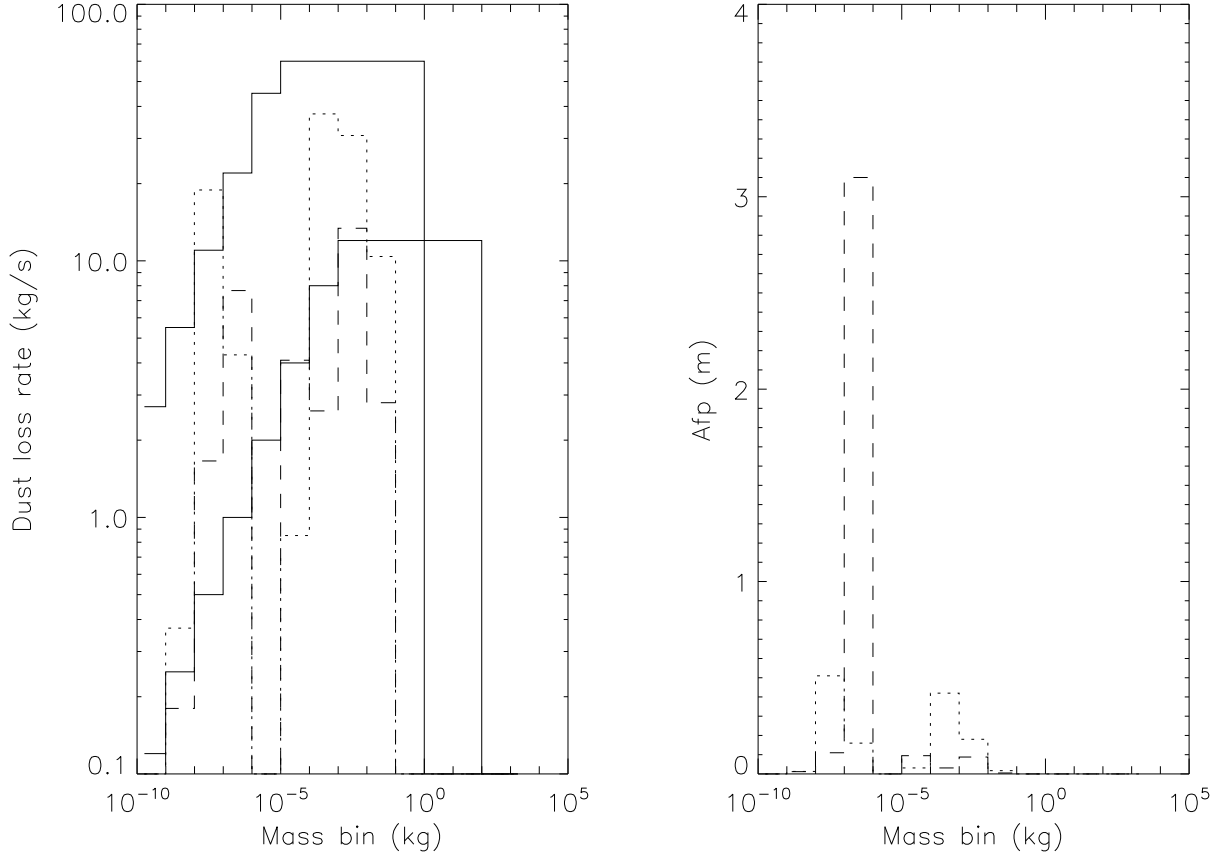


Fig. 5.— 67P dust mass distribution at 2.1 au pre-perihelion. Left panel, continuous lines: upper and lower limits of the predicted dust loss rate (Fulle et al. 2010). The power index of the associated differential size distribution is  $-3$  below  $10^{-6}$  kg and  $-4$  above  $10^{-5}$  kg. Left panel, dashed line: observed dust loss rate (39 GIADA detections on 28 March 2015 in the 3 lower mass bins; and 74 OSIRIS detections in the 4 upper mass bins, assumed bulk density of  $10^3$  kg  $m^{-3}$ ; data in Tab. 6). Left panel, dotted line: observed dust loss rate (81 GIADA data on 13-17 March 2015 in the 3 lower mass bins; and 74 OSIRIS detections in the 4 upper mass bins, assumed bulk density of  $3 \times 10^3$  kg  $m^{-3}$ ; data in Tab. 7). Right panel: observed  $Af\rho$  (GIADA detections in the 3 lower mass bins, OSIRIS detections in the 4 upper mass bins; dashed line, assumed dust bulk density of  $10^3$  kg  $m^{-3}$ ; dotted line, assumed dust bulk density of  $3 \times 10^3$  kg  $m^{-3}$ ). The total dust loss rate is  $70 \pm 30$  kg  $s^{-1}$ . The total  $Af\rho$  is  $2.3 \pm 1.0$  m.



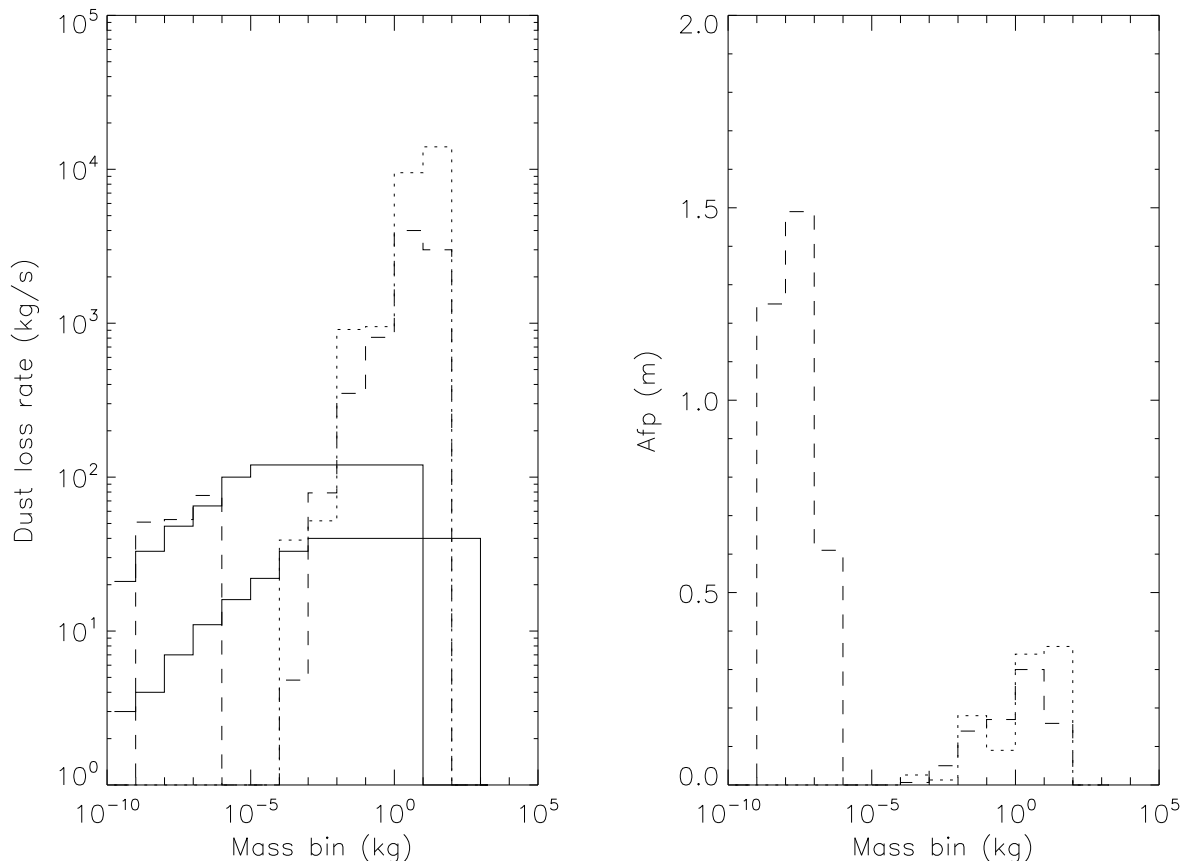


Fig. 6.— 67P dust mass distribution at perihelion. Left panel, continuous lines: upper and lower limits of the predicted dust loss rate (Fulle et al. 2010). The power index of the associated differential size distribution is  $-3.6$  below  $10^{-6}$  kg and  $-4$  above  $10^{-5}$  kg. Left panel, dashed line: observed dust loss rate (124 GIADA detections in the 3 lower mass bins; and 102 OSIRIS detections in the 6 upper mass bins, assumed bulk density of  $10^3$  kg m $^{-3}$ , data in Tab. 8). Left panel, dotted line: 102 OSIRIS detections in the 6 upper mass bins, assumed bulk density of  $3 \times 10^3$  kg m $^{-3}$ ). Right panel: observed  $Af\rho$  (GIADA in the 3 lower mass bins, OSIRIS in the 6 upper mass bins; dashed line, assumed dust bulk density of  $10^3$  kg m $^{-3}$ ; dotted line, assumed dust bulk density of  $3 \times 10^3$  kg m $^{-3}$ ). The total dust loss rate is  $(1.7 \pm 0.9) \times 10^4$  kg s $^{-1}$  in all mass bins, and  $(1.5 \pm 0.5) \times 10^3$  kg s $^{-1}$  excluding dust of mass  $> 1$  kg. The total  $Af\rho$  is  $4.3 \pm 0.1$  m.

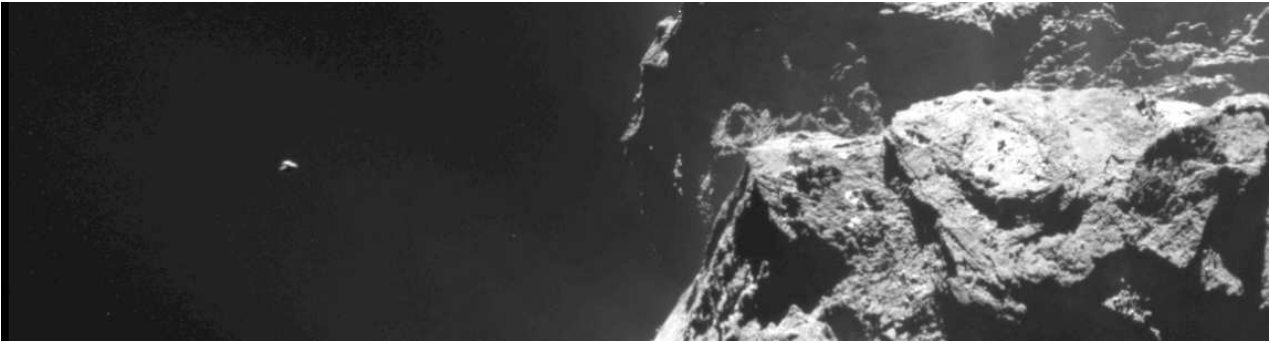


Fig. 7.— Resolved boulder (on the left) observed by OSIRIS NAC camera on 30 July 2015, 22h07m UT. Nucleus distance  $R = 180$  km, boulder at  $D = 3.5$  km and of radius  $r = 0.4$  m. 67P nucleus on the right.